

Florida Institute of Technology

## Scholarship Repository @ Florida Tech

---

Theses and Dissertations

---

12-2023

### Low Reynolds Number Locomotion Near Interfaces in Two-fluid Media

Avriel Rowena Mae Cartwright

Florida Institute of Technology, [acartwright2017@my.fit.edu](mailto:acartwright2017@my.fit.edu)

Follow this and additional works at: <https://repository.fit.edu/etd>



Part of the [Applied Mathematics Commons](#)

---

#### Recommended Citation

Cartwright, Avriel Rowena Mae, "Low Reynolds Number Locomotion Near Interfaces in Two-fluid Media" (2023). *Theses and Dissertations*. 1391.

<https://repository.fit.edu/etd/1391>

This Dissertation is brought to you for free and open access by Scholarship Repository @ Florida Tech. It has been accepted for inclusion in Theses and Dissertations by an authorized administrator of Scholarship Repository @ Florida Tech. For more information, please contact [kheifner@fit.edu](mailto:kheifner@fit.edu).

Low Reynolds Number Locomotion Near Interfaces in Two-fluid Media

by

Avriel Rowena Mae Cartwright

Bachelor of Science  
Mathematics  
University of The Bahamas  
2017

Bachelor of Education  
Secondary Certification: Mathematics  
University of The Bahamas  
2017

A dissertation  
submitted to the College of Engineering and Science  
at Florida Institute of Technology  
in partial fulfillment of the requirements  
for the degree of

Doctor of Philosophy  
in  
Applied Mathematics

Melbourne, Florida  
December, 2023

© Copyright 2023 Avriel Rowena Mae Cartwright  
All Rights Reserved

---

The author grants permission to make single copies.

We the undersigned committee  
hereby approve the attached dissertation

Low Reynolds Number Locomotion Near Interfaces in Two-fluid Media by

Avriel Rowena Mae Cartwright

---

Jian Du, Ph.D.  
Associate Professor  
Mathematics and Systems Engineering

---

Venkat Keshav Chivukula, Ph.D.  
Assistant Professor  
Biomedical Engineering and Science

---

Gnana Bhaskar Tenali, Ph.D.  
Professor and Department Head  
Mathematics and Systems Engineering

---

Aaron Welters, Ph.D.  
Assistant Professor  
Mathematics and Systems Engineering

# Abstract

Title:

Low Reynolds Number Locomotion Near Interfaces in Two-fluid Media

Author:

Avriel Rowena Mae Cartwright

Major Advisor:

Jian Du, Ph.D.

Microorganisms often swim within complex fluid environments composed of multiple materials with very different properties. Biological locomotion, including swimming speed, is significantly impacted by the physical composition and rheology of the surrounding fluid environment, as well as the presence of phase boundaries and free interfaces, across which physical properties of the fluid media may vary greatly. Through computational simulations, we first investigate the classical Taylor's swimming sheet problem near interfaces within multi-fluid environments using a two-fluid immersed boundary method. The accuracy of the methodology is illustrated through comparisons with analytical solutions. Our simulation results indicate that the interface dynamics and phase separation in the multi-fluid mixture are closely coupled with the movement of the swimmer. Depending on the interface location, the frictional coefficient, and the multi-fluid composition, the swimmer can move either faster or slower than that in a single-phase fluid. Furthermore, we investigate the movement of a finite-length

undulatory swimmer near interfaces within a viscous two-fluid media. Our simulation results show that significant speed-ups can be achieved only if the active swimmer has a large body elasticity.

# Table of Contents

<b>Abstract</b> . . . . .	iii
<b>List of Figures</b> . . . . .	vii
<b>List of Tables</b> . . . . .	x
<b>1 Introduction</b> . . . . .	1
<b>2 Model Equations and Numerical Method</b> . . . . .	10
2.1 Two-Fluid Mixture Model . . . . .	11
2.2 Immersed Boundary Method for Multi-Fluid Mixture . . . . .	14
2.2.1 Model of Infinite Swimmer . . . . .	14
2.2.2 Model of Finite Swimmer . . . . .	17
2.3 Computational Discretization . . . . .	19
2.4 Numerical Solutions . . . . .	25
<b>3 Results</b> . . . . .	27
3.1 Locomotion of Infinite Swimmer Near Interfaces . . . . .	27
3.1.1 Problem Setup . . . . .	27
3.1.2 Comparison with Analytic Solutions . . . . .	29
3.1.3 Swimming Near Non-Deformable Fluid Interface . . . . .	29

3.1.4	Swimming Near Deformable Fluid Interface . . . . .	32
3.1.5	Force Analysis . . . . .	36
3.1.6	Swimming Near Deformable Interface in Fluid Mixtures . . . . .	40
3.2	Locomotion of Finite Swimmer Near Interfaces . . . . .	48
3.2.1	Problem Setup . . . . .	48
3.2.2	Soft Swimmer Near Fluid Interface . . . . .	49
3.2.3	Stiff Swimmer Near Fluid Interface . . . . .	50
<b>4</b>	<b>Conclusion . . . . .</b>	<b>53</b>
	<b>References . . . . .</b>	<b>57</b>

# List of Figures

1.1	Illustration representing biological swimmers on different length scales. The swimmer velocity and Reynolds number changes with length scale. [2]. . . . .	2
1.2	<i>H. Pylori</i> crossing mucus layer of stomach [1]. According to [6], gastric mucin forms a gel at $\text{pH} < 4$ . <i>H. pylori</i> cannot move in mucin gels and so secretes urease that hydrolyzes urea to produce ammonia. This elevates the pH which de-gels the mucin, enabling the bacterium to swim in the resulting polymer solution. The picture, not copyrighted, is reproduced from an NSF press release 09-149. <a href="https://www.nsf.gov/news/news_summ.jsp?cntn_id=115409&amp;org=NSF&amp;from=news">https://www.nsf.gov/news/news_summ.jsp?cntn_id=115409&amp;org=NSF&amp;from=news</a> . . . . .	5
2.1	Two-Fluid Mixture Model: The outer red sections represent the more viscous fluid component, the network phase, and the inner blue section represents the less viscous fluid, the solvent phase. The black curve represents the immersed structure (the swimmer). . . . .	12
2.2	Dual IB representation of a swimmer. $\bullet - \mathbf{X}_n(q, t)$ , $\circ - \mathbf{X}_s(q, t)$ . . . . .	15
2.3	Model of Finite Swimmer: The swimmer (represented by the black curve) moves in a low-viscosity region, solvent phase (represented by the blue region), surrounded by a more viscous bulk fluid, network phase (represented by the red region). . . . .	17

2.4	Spreading of force in the $x$ -direction. . . . .	21
2.5	Spreading of force in the $y$ -direction. . . . .	22
2.6	MAC-Type Staggered Computational Grid. . . . .	24
3.1	Distribution of network volume fraction $\theta_n$ and fluid velocity $\mathbf{u}_s$ at $t = 0.5$ for different $H$ . All vectors have the same scale. The viscosity ratio between the two fluids is $\beta = 0.5$ . . . . .	31
3.2	The scaled swimming speed vs. the nondimensional interface height $kH$ for different $\beta$ . The fluid interfaces are non-deformable. The analytical solutions are from [26]. . . . .	31
3.3	Distribution of network volume fraction $\theta_n$ and fluid velocity $\mathbf{u}_s$ at $t = 0.5$ for different $H$ . All vectors have the same scale. The viscosity ratio between the two fluids is $\beta = 0.5$ . . . . .	34
3.4	Distribution of network volume fraction $\theta_n$ and fluid velocity $\mathbf{u}_s$ at $t = 0.5$ for different $H$ . All vectors have the same scale. The viscosity ratio between the two fluids is $\beta = 0.1$ . . . . .	34
3.5	$H = 0.16$ . Distributions of $\mathbf{u}_s$ , the profiles of swimming sheet (black curves) and fluid interfaces (red curves) for different $\beta$ . ( <b>a,c,e,g</b> ) are for $\beta = 0.5$ . ( <b>b,d,f,h</b> ) are for $\beta = 0.1$ . All vectors have the same scale. . . . .	35
3.6	The scaled swimming speed vs. the nondimensional interface height $kH$ for different $\beta$ . The fluid interfaces are deformable. The analytical solutions are from [10]. . . . .	36
3.7	Thrust and drag coefficient vs. the nondimensional interface height $kH$ . $\beta = 0.5$ . The fluid interfaces are not deformable. . . . .	38
3.8	Thrust and drag coefficient vs. the nondimensional interface height $kH$ for different $\beta$ . The fluid interfaces are deformable. . . . .	39

3.9	Comparison of the effect of interface rigidity: Thrust force vs. the nondimensional interface height $kH$ for non-deformable vs. deformable interface. $\beta = 0.5$ . . . . .	40
3.10	$H = 0.16$ , $\beta = 0.25$ , $\xi = 100$ , $\theta_n^{in} = 0.2$ , and $\theta_n^{out} = 0.8$ . Distributions of $\theta_n$ and $\mathbf{u}_n$ at different times. All vectors have the same scale. . . . .	43
3.11	$H = 0.16$ , $\beta = 0.25$ , $\xi = 100$ , $\theta_n^{in} = 0.2$ , and $\theta_n^{out} = 0.8$ . Distributions of $\theta_n$ and $\mathbf{u}_s$ at different times. All vectors have the same scale. . . . .	44
3.12	Effect of frictional coefficient: $H = 0.16$ , $\beta = 0.25$ , $\theta_n^{in} = 0.2$ , and $\theta_n^{out} = 0.8$ . Distributions of $\theta_n$ and velocity difference $\mathbf{u}_n - \mathbf{u}_s$ at $t = 1.0$ . All vectors have the same scale. . . . .	44
3.13	Effect of interface location $H$ : $\beta = 0.25$ , $\xi = 100$ , $\theta_n^{in} = 0.2$ , and $\theta_n^{out} = 0.8$ . Distributions of $\theta_n$ and $\mathbf{u}_s$ at different times. All vectors have the same scale. . . . .	45
3.14	The scaled swimming speed vs. $\theta_n^{in}$ for different $H$ and $\xi$ . $\beta = 0.25$ and $\theta_n^{out} = 0.8$ . The analytical solutions are from [10]. . . . .	47
3.15	Soft Swimmer . . . . .	51
3.16	Stiff Swimmer . . . . .	52

# List of Tables

3.1	Relative errors of the simulated swimming speed for different $\beta$ and nondimensional interface height $kH$ . The fluid interfaces are non-deformable. The analytical solutions are from [26]. . . . .	32
3.2	Relative errors of the simulated swimming speed for different $\beta$ and nondimensional interface height $kH$ . The fluid interfaces are deformable. The analytical solutions are from [10]. . . . .	36
3.3	Non-deformable interface ( $\beta = 0.5$ ): thrust force, drag coefficient, their ratio, and the simulated swimming speed. . . . .	37
3.4	Deformable interface ( $\beta = 0.5$ ): thrust force, drag coefficient, their ratio, and the simulated swimming speed. . . . .	37

# Chapter 1

## Introduction

In recent years, there has been increased research interest concerning the locomotion of microorganisms within their surrounding fluid environment. This field of study delves into the intricate movements exhibited by microorganisms as they navigate through their habitats. From the swimming of spermatozoa which fuse with ova during fertilization [3], to the navigation of the ulcer-causing *Helicobacter pylori* through the gastric mucus layer [6], and the run-and-tumble dynamics of *Escherichia coli* in polymeric solutions [30], the investigation of microorganism locomotion opens a portal to understanding fundamental biological processes and potential biomedical applications.

Microorganisms are ubiquitous, existing in diverse ecological niches ranging from aquatic environments to living organisms. The physics governing swimming behavior at the microscale fundamentally differ from that observed at the macroscopic level. The significance of this difference is primarily due to the dominance of viscous damping over inertia - a defining characteristic of low Reynolds number swimming. The investigation of this phenomenon has both biological and pathological significance as key processes such as reproduction and bacterial infection depend on the ability of microorganisms to efficiently navigate their surroundings making these processes have far-reaching im-

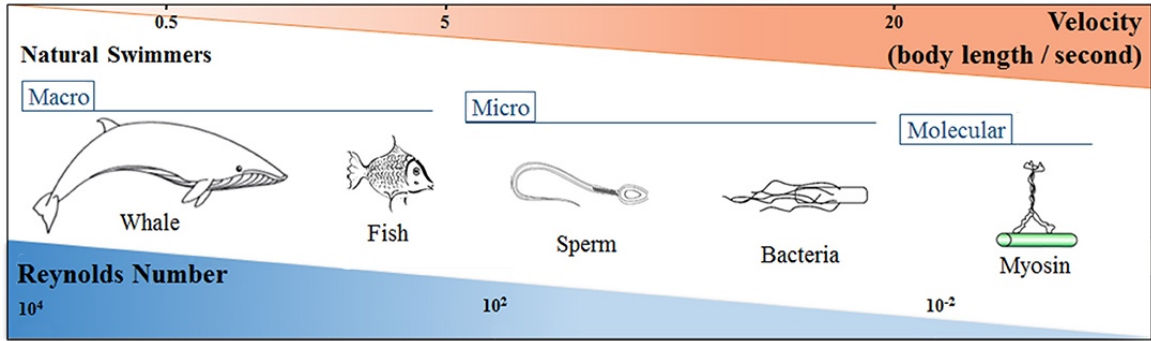


Figure 1.1: Illustration representing biological swimmers on different length scales. The swimmer velocity and Reynolds number changes with length scale. [2].

plications for human health. Studies are further motivated by the potential biomedical applications, such as the design of synthetic micro-swimmers for targeted drug delivery and cargo towing.

While the mechanics of microorganism locomotion in a single phase Newtonian fluid has been studied extensively, and the underlying dynamics are well understood, the fluidic environments inhabited by microorganisms are often far from homogeneous. Many biological fluids, such as mucus and cytoplasm, are mixtures of water and polymer network. These multi-phase fluid mixtures, called complex fluids, generally exhibit complicated non-Newtonian characteristics and have introduced new complexities to this field of study. The composition and rheology of such fluid mixtures have a significant impact on the speed and efficiency of biological locomotion. Recent experimental studies have provided new insights into the mechanics behind small scale swimming in complex fluids.

On the other hand, mathematical modeling, analysis, and computational simulations are playing more important roles in the investigation of the mechanics behind small-scale swimming in complex multiphase fluids [16][21]. Early research efforts were centered on the effect of fluid properties, such as elasticity, on idealized swimmers who exhibited propulsion gaits independent of the surrounding fluid. Recently, interesting

features with more biological relevance have been revealed about the dynamics of undulatory swimmers. A notable example lies in the study of viscoelastic stresses, which have been shown to induce larger waving amplitudes and enhanced swimming speed in flexible swimmers driven by prescribed spatio-temporal internal actuation [32]. For finite swimmers with imposed active body moment density, the role of elasticity becomes even more intriguing, with the potential to either enhance or hinder swimming motion depending on factors such as body stiffness and swimming stroke [39]. Such discoveries underscore the intricate interplay between fluid properties and microorganism dynamics, revealing a nuanced relationship that influences swimming behavior.

The presence of physical boundaries and material interfaces in the vicinity of swimming microorganisms has also emerged as a crucial determinant of their swimming behavior. The proximity to these interfaces bestows upon microorganisms a unique set of behaviors. The bacterium, *Escherichia coli*, (abbreviated as *E. coli*), which is commonly found in the environment, foods, and intestines of humans and animals, has been used as a prototypical micro-swimmer for studying these characteristics. In solution, *E. coli* cells move in a run-and-tumble fashion as they swim in a random walk pattern, characterized by approximately straight swimming trajectories alternating with rapid re-orientations. In [22], a hydrodynamic model for the motion of *E. coli* near solid boundaries is presented. Their results reveal that near a solid boundary, *E. coli* adopts clockwise circular trajectories as a result of force-free and torque-free swimming and the hydrodynamic interactions with the boundary. These interactions lead to a hydrodynamic trapping of cells close to the surface which further results in cells remaining in close proximity to the surface for long time periods. This enhances the probability of cell adhesion to substrates. This behavior is both biologically and pathologically significant in the initial stages of biofilm formation and pathogenic infections. It also holds practical applications in biotechnology and microfluidics. The run-and-tumble

dynamics of *E. coli* is further studied in [30] with a focus on polymeric solutions. Their results reveal that even small amounts of polymer in solution can significantly impact *E. coli* swimming dynamics. Cells tumble less while velocity increases. This results in an enhancement in cell translational diffusion and a significant decline in rotational diffusion. The decrease of tumbling is a result of fluid viscosity while swimming speed enhancement is primarily due to fluid elasticity. Loss of rotational diffusion ultimately decreases the time cells spend in close proximity to the boundary and so offers the conclusion that the material properties of a fluidic environment can control spreading of bacteria.

Similarly, the swimming behaviors of spermatazoa near solid and free surfaces is explored in [3]. The goal of this study is to evaluate the influence of proximity to surfaces on the movement of sterlet spermatazoa. It was observed that sperm cells near a liquid-solid interface swim slower than those near a liquid-gas interface and that proximity to a surface possibly causes rotation. The investigation of microorganism locomotion in heterogeneous fluid environments also reveals an interesting facet of swimming dynamics - the ability of some micro-swimmers to significantly enhance their motility by creating heterogeneous layers of fluids around them. This is evident in the case of self-propelling helical swimmers in shear-thinning fluids. In [19], the impact of a controlled variation of the rheological parameters of shear-thinning fluids on well-defined swimming strategies is explored. Their results reveal that self-propelling helical swimmers in shear-thinning fluids may move 50% faster than in a Newtonian fluid. This speedup is believed to be a result of the viscosity stratification around the swimmer. Similarly, the interaction between the ulcer-causing gastric pathogen, *Helicobacter pylori* (abbreviated as *H. pylori*), and gastric mucin demonstrate how the transition of fluid composition from a viscoelastic gel to a viscous fluid may profoundly affect the bacteria's locomotion. *H. pylori* is the only bacterium known to colonize

the harsh acidic environment of the human stomach. In [6], the movement of *H. pylori* through the viscoelastic mucus gel that coats the stomach wall is studied. This viscoelastic gel, gastric mucin, forms a layer of protective gel for the stomach lining against harmful bacteria. Their results reveal that to swim through the mucus layer, *H. pylori* alters the rheological properties of its environment by hydrolyzing ambient urea to produce ammonia. This results in an elevation of pH, and the transition of local gastric mucus from a viscoelastic gel to a viscous fluid. Therefore, the bacterium essentially swims through a pocket of fluid surrounded by mucus gel which ultimately enables it to attach to epithelial cells and cause infection (see Figure 1.2).

### **H. PYLORI CROSSING MUCUS LAYER OF STOMACH**

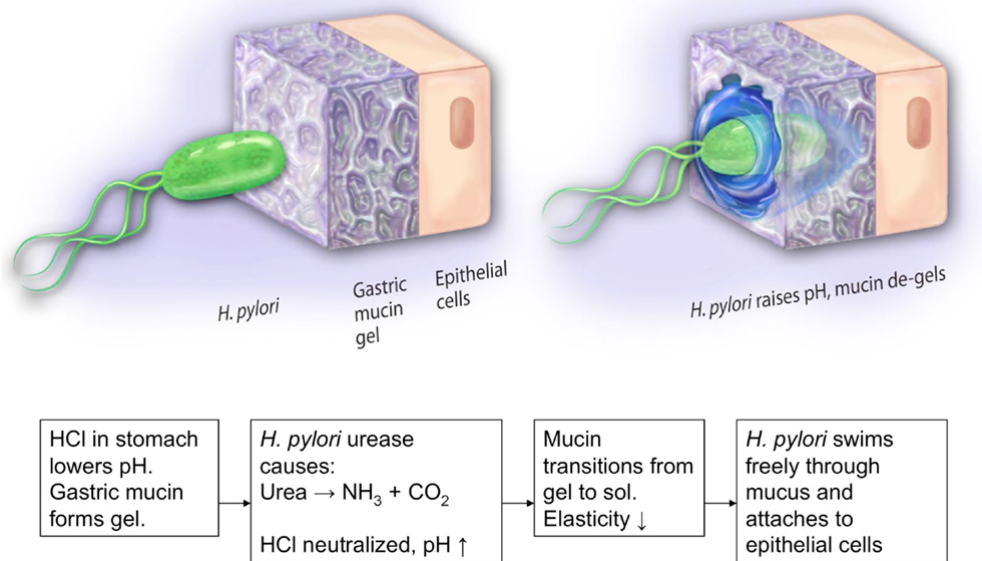


Figure 1.2: *H. Pylori* crossing mucus layer of stomach [1]. According to [6], gastric mucin forms a gel at  $\text{pH} < 4$ . *H. pylori* cannot move in mucin gels and so secretes urease that hydrolyzes urea to produce ammonia. This elevates the pH which de-gels the mucin, enabling the bacterium to swim in the resulting polymer solution. The picture, not copyrighted, is reproduced from an NSF press release 09-149. [https://www.nsf.gov/news/news\\_summ.jsp?cntn\\_id=115409&org=NSF&from=news](https://www.nsf.gov/news/news_summ.jsp?cntn_id=115409&org=NSF&from=news)

Motivated by these experimental discoveries, there have been a number of theoretical analyses on the dynamics of micro-swimmers near fluid interfaces. In [33], the interaction between a swimming sheet and a plane surfactant-laden interface is investigated. Their results reveal that the uniformity of swimming speed near a surfactant-laden interface may differ from that observed near a clean interface. This disparity is highly contingent on the wave type traversing the sheet. Exploring the realm of viscous fluid environments, [29] presents a theoretical locomotion model that investigates the impact of heterogeneity generated by a spherical swimmer on its swimming characteristics within a viscous fluid surrounded by a Brinkman medium. Their results reveal that heterogeneity influences the propulsion performance of the swimmer. Additionally, they find that depending on the surface velocities and fluid properties, there exists a minimum threshold size of mucus gel that a swimmer must liquify in order to achieve any enhancement in swimming speed. This threshold size can be as much as approximately 30% of the swimmer's size.

In [10], the speed of an infinitely long swimmer in close proximity to an elastic deformable membrane within two layers of fluids is studied. Results reveal that differing viscosities on either side of the flexible interface can lead to fluid pumping along or against the swimming direction, depending on which viscosity is greater. Transitioning to the investigation of swimmers near stationary interfaces, [26] proposes a physical mechanism for locomotion enhancement of microscopic swimmers within complex fluids. Their results reveal that phase-separation systematically enhances swimming speeds, possibly by orders of magnitude. Furthermore, this phase-separation emerges as a potential contributor to the recently measured swimming enhancement at low-Reynolds numbers.

Theoretical studies such as those discussed offer valuable information for the locomotion of micro-swimmers. The discoveries enable researchers to isolate and examine

specific factors that influence the mechanics of locomotion of these organisms. The flexibility of theoretical models facilitates the exploration of a wide range of parameters, allowing researchers to examine scenarios which may be difficult to recreate experimentally. Despite the advantages, these studies are not without their drawbacks. The complex interactions between fluid dynamics and microorganism locomotion can be difficult to capture in a theoretical framework. Theoretical studies often require simplifications and assumptions which may deviate from the complexity of real-world scenarios. These idealizations might overlook critical aspects which influence microorganism locomotion or may be tailored to specific microorganism types or fluid properties which can limit the extension of findings to a broader range of organisms and environments. Furthermore, theoretical studies are limited in their biological relevance. For example, these studies can only account for infinite swimmers with small amplitude in simple fluid environments.

Relative to the numerous theoretical studies, there are only a few computational investigations on locomotion of micro-organisms within a multi-component fluid. This is mainly due to the numerical challenges associated with the simulation of multi-fluid mixtures separated by dynamical boundaries. In [13], an extension of the classic Immersed Boundary (IB) Method is presented. The interactions between elastic boundaries and mixtures of two fluids is simulated, with both fluids satisfying the no-slip condition on the immersed structures. The observation was that for the classical Taylor's sheet within a two viscous fluids mixture, the swimming speed is always less than that in a single phase viscous fluid. A more general framework based on IB Method was developed in [24] for the investigation of elastic swimmers within viscoelastic fluid mixtures. However, no free interfaces are included in these studies.

Computational studies such as those outlined offer numerous advantages. They allow for the simulation of complex and realistic fluid environments, delivering a more

accurate representation of microorganism locomotion compared to a simplified theoretical model. These models and simulations allow for extensive parameter exploration providing insights into microorganism behavior under diverse scenarios. These factors, combined with the ability to achieve high spatial and temporal resolution, allows for detailed analysis of microorganism dynamics and their interactions with fluid media. Furthermore, these models serve as predictive tools, guiding experimental design.

This dissertation contributes to the growing body of knowledge by delving into the dynamics of microorganism locomotion near interfaces within a two-fluid environment. By employing the computational method developed in [13], in our work, we investigate the classical Taylor’s swimming sheet problem near interfaces in a heterogeneous two-fluid environment [4]. Our mixture model provides a simple and unified framework for the study of swimming dynamics near interfaces in a multi-fluid mixture. The swimmer moves in a low-viscosity region surrounded by a more viscous bulk fluid, with different fluid layers separated by interfaces. Explicit interface tracking is avoided through a numerical regularization, which significantly simplifies the algorithm implementation, particularly for problems involving dynamic interfaces. To the best of our knowledge, this is the first time that such problems are simulated by a combination of the IB method and the interface-capturing strategy. Our work also sheds light on locomotion characteristics within heterogeneous fluid media. The results of our simulations show that swimmers in a two-fluid mixture near free interfaces may move faster or slower than that in a single fluid depending on their distance from the interface, the composition of the fluid mixture, and the magnitude of the frictional force between components in the mixture.

We have also conducted the first computational investigation on the locomotion of a finite-length undulatory swimmer near interfaces in viscous two-fluid mixtures [5]. In this study, the swimmer is in a low-viscosity fluid surrounded by a more viscous bulk

flow. To drive the motion of the swimmer, we use the methodology proposed in [21]. Instead of swimming with a specified gait, the swimmer is actuated by a prescribed active body moment density. Our simulation results reveal that relative to its motion in a single fluid, a swimmer with large body elasticity can move much faster near fluid interfaces in a two-fluid domain. In contrast, the speed of a soft swimmer is not significantly affected by the presence of fluid interfaces. The computational framework presented can be applied to the study of locomotion of microorganisms within various biofluid media, particularly for cases where swimmers are in close proximity to free deformable interfaces. The flexibility of our method also makes it a suitable tool to investigate problems in which structural properties of the fluid media are altered by the dynamic of the swimmer. One such example is the ulcer-causing pathogen *H. pylori*.

The rest of the dissertation is organized as follows. In Chapter 2, the model equations and numerical methods are presented. This is followed by Chapter 3 where the results of the simulations are presented and analyzed. In Chapter 4, discussions about the results and potential extensions of the computational method are given.

## Chapter 2

# Model Equations and Numerical Method

Many biological fluids, such as biofilms, blood clots, mucus, and cytoplasm, are composed of a polymer network immersed in a solvent. In many cases, these complex fluids are not sufficiently described as a single continuous medium due to the multiscale and multicomponent nature of the materials. This introduces various mathematical, modeling, and computational challenges that extend beyond traditional fluid mechanics. Standard single-phase fluid models may face significant limitations when attempting to capture the underlying biological processes, primarily because they assume that all species move in the same velocity field. However, this assumption is not biologically relevant as different species may move in different velocity fields. Two additional limitations of these single-phase descriptions are that these processes are frequently driven by the relative motion of the different components of the fluid, and the composition of the material may be dynamic. As a result, modeling the fluid mechanics of this process requires a description beyond a single velocity field and single stress tensor. A

more suitable and biologically relevant approach to describe these problems involves the two-phase (multiphase) flow model. In this model, both polymer network and solvent coexist at each point of space simultaneously. Each phase, namely the network and the solvent, is modeled as a distinct continuum with its own velocity field and constitutive law. Two sets of momentum equations govern the two velocity fields with each involving the stresses appropriate for the respective material.

## 2.1 Two-Fluid Mixture Model

In our work, we employ the computational methodology developed in [13]. The swimmer moves within a two-fluid domain where the thin fluid layer of low viscosity in direct contact with the swimmer is enclosed by a more viscous bulk fluid. Two-fluid models of this kind have been successfully used for the investigation of many bio-fluids such as blood clots, bio-film, and cytoplasm [12, 8]. This type of model also holds significant biological relevance as it relates to the study of locomotion of microorganisms within various biofluid media, particularly for the cases where swimmers are near free deformable interfaces and are able to alter the structural properties of the fluid media. For example, gastric mucin transitions from a viscoelastic gel to a viscous solution, triggered by the urease production from the ulcer-causing pathogen, *H. pylori*. This localized de-gelling process essentially allows the bacterium to swim through a pocket of fluid, surrounded by gel, and cause infection.

For simplicity of discussion, we call the less viscous fluid in the mixture as the solvent phase (denoted by  $s$ ), and the more viscous fluid component as the network phase (denoted by  $n$ ). We treat the fluid medium surrounding the swimmer as a mixture of two immiscible fluids to avoid tracking the interfaces between fluid layers explicitly (see Figure 2.1).

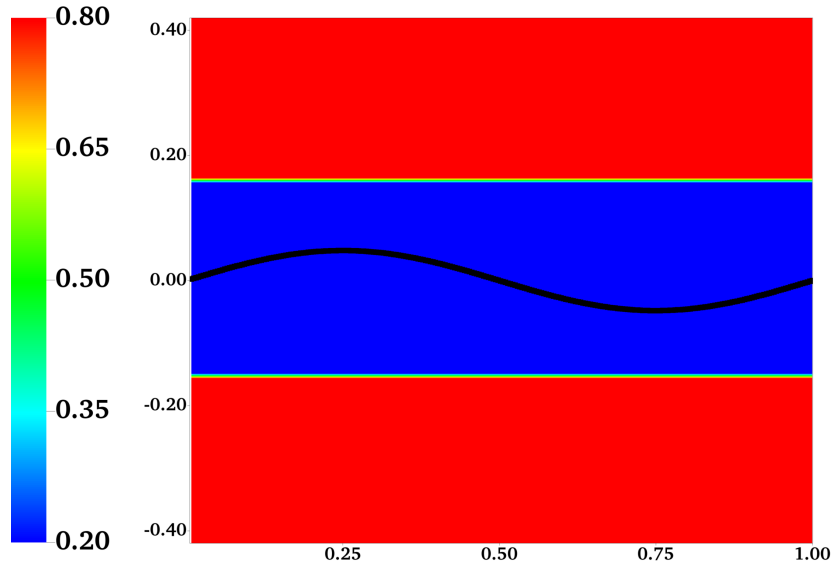


Figure 2.1: Two-Fluid Mixture Model: The outer red sections represent the more viscous fluid component, the network phase, and the inner blue section represents the less viscous fluid, the solvent phase. The black curve represents the immersed structure (the swimmer).

At any given spatial location  $\mathbf{x}$ , the relative quantities of the solvent and network are represented by their volume fractions, denoted by  $\theta_s(\mathbf{x}, t)$  and  $\theta_n(\mathbf{x}, t)$ . The solvent and network fluids move with their own velocity fields,  $\mathbf{u}_s(\mathbf{x}, t)$  and  $\mathbf{u}_n(\mathbf{x}, t)$ :

$$\frac{\partial \theta_s}{\partial t} + \nabla \cdot (\theta_s \mathbf{u}_s) = 0, \quad (2.1)$$

$$\frac{\partial \theta_n}{\partial t} + \nabla \cdot (\theta_n \mathbf{u}_n) = 0. \quad (2.2)$$

Since  $\theta_n + \theta_s = 1$ , adding (2.1) and (2.2) gives the volume averaged incompressibility condition:

$$\nabla \cdot (\theta_s \mathbf{u}_s + \theta_n \mathbf{u}_n) = 0. \quad (2.3)$$

For a small Reynolds number, the force balance equations for the two fluids are given

by:

$$\nabla \cdot (\theta_s \sigma_s) - \theta_s \nabla p + \xi \theta_n \theta_s (\mathbf{u}_n - \mathbf{u}_s) + \mathbf{f}_s = 0, \quad (2.4)$$

$$\nabla \cdot (\theta_n \sigma_n) - \theta_n \nabla p + \xi \theta_n \theta_s (\mathbf{u}_s - \mathbf{u}_n) + \mathbf{f}_n = 0. \quad (2.5)$$

Here,  $\sigma_s$  and  $\sigma_n$  are the viscous stress tensors for the solvent and network fluids, respectively.  $p$  is the pressure. The frictional drag force between the two fluids due to relative motions is calculated as  $\xi \theta_n \theta_s (\mathbf{u}_n - \mathbf{u}_s)$  with  $\xi$  being the frictional coefficient. The force densities generated by immersed elastic structures, which in our work is the swimmer, on the two fluids are denoted by  $\mathbf{f}_s$  and  $\mathbf{f}_n$ . The viscous stress tensors are taken to be those of the Newtonian fluids:

$$\sigma_s = \mu_s (\nabla \mathbf{u}_s + \nabla \mathbf{u}_s^T) + (\lambda_s \nabla \cdot \mathbf{u}_s) I, \quad (2.6)$$

$$\sigma_n = \mu_n (\nabla \mathbf{u}_n + \nabla \mathbf{u}_n^T) + (\lambda_n \nabla \cdot \mathbf{u}_n) I. \quad (2.7)$$

Here,  $I$  is the identity tensor. The shear viscosities for the solvent and network are denoted as  $\mu_s$  and  $\mu_n$ , respectively.  $\lambda_{s,n} + 2\mu_{s,n}/d$  is the bulk viscosity of the solvent and network ( $d$  is the space dimension). We set the second viscosity coefficients of the two fluids as  $\lambda_{s,n} = -\mu_{s,n}$  so that the bulk viscosities for both fluids are zero. Conceptually, we have  $\theta_n = 0$  for the inner fluid layer surrounding the swimmer and  $\theta_n = 1$  for the bulk fluid. Due to the degeneracy of equations (2.4) and (2.5) from these conditions, we use approximated general conditions for all simulations as discussed later. We nondimensionalize all model equations using the characteristic length scale of  $L = 1$   $\mu\text{m}$ , time scale of  $T = 1$  second, and stress scale of  $\mu_s/T$ . The viscosity of the solvent,  $\mu_s$ , is taken as the viscosity of water.

## 2.2 Immersed Boundary Method for Multi-Fluid Mixture

The Immersed Boundary (IB) Method is a powerful computational tool for handling the dynamic interactions between fluids and immersed elastic structures [31]. The simplicity and robustness of the IB method has resulted in its numerous applications in biological problems (see [38]-[18]). In [13], an extension of this method to a two-phase fluid is developed. We employ this computational methodology in our work, in which a two-phase IB scheme is used for the simulation of interactions between elastic structures and a two-fluid mixture.

In our work, we investigate the movement of two types of swimmers - swimmers of infinite length and swimmers of finite length. Although the concept of swimmers with infinite length may not hold biological relevance, we include them in our study due to existing theoretical studies, specifically those presented in [10] and [23], with which we can directly compare our findings. This comparative analysis serves as a means to gauge the accuracy and validity of our model. In addition to the infinite swimmers, we also investigated the dynamics of finite swimmers near fluid interfaces, whose movements are driven by a prescribed target curvature. The swimming gait of these swimmers is a direct result of the fluid-structure interactions of the swimmer with its surrounding fluid environment, making the study of these swimmers more biologically relevant. The following sections will provide a more comprehensive exploration of each of our swimmer models.

### 2.2.1 Model of Infinite Swimmer

In the two-phase IB scheme, an Eulerian description is used for the fluid variables such as velocity and pressure, while a Lagrangian description is used for the immersed

structures. Each immersed structure is represented by two immersed boundaries, denoted by  $\Gamma^n$  (network IB) and  $\Gamma^s$  (solvent IB), respectively. As shown in Figure 2.2, the spatial locations of IB points on  $\Gamma^n$  and  $\Gamma^s$  are represented by the vector functions  $\mathbf{X}_n(q, t)$  and  $\mathbf{X}_s(q, t)$  respectively. Here,  $q \in [0, L]$  is the Lagrangian coordinate and  $L$  represents the length of the swimmer. At initial time, we have  $\mathbf{X}_n(q, 0) = \mathbf{X}_s(q, 0)$ .

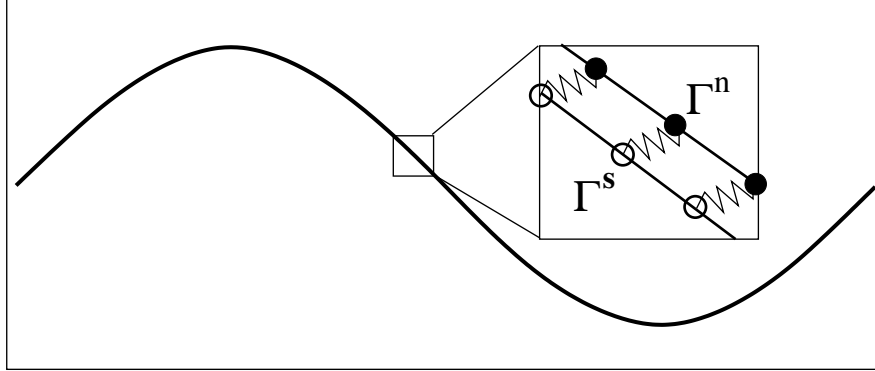


Figure 2.2: Dual IB representation of a swimmer.  $\bullet$  –  $\mathbf{X}_n(q, t)$ ,  $\circ$  –  $\mathbf{X}_s(q, t)$ .

In our work investigating the movement of a swimmer of infinite length [4], both the solvent and the network satisfy the non-slip condition on the immersed structure. That is, the IB points on  $\Gamma^n$  move with the local network velocity  $\mathbf{u}_n$ , while the IB points on  $\Gamma^s$  move with the local solvent velocity  $\mathbf{u}_s$ . To prevent  $\Gamma^n$  and  $\Gamma^s$  from separating, the pairs of corresponding IB points on them is connected by a stiff spring with zero rest length (see Figure 2.2). Penalty forces equal in magnitude with opposite directions are generated at these two points when their spatial locations differ. The penalty force density at  $\mathbf{X}_n$  is computed by  $\mathbf{F}_n^p = k_p(\mathbf{X}_s - \mathbf{X}_n)$ , where  $k_p$  is the penalty spring constant. The penalty force density  $\mathbf{F}_s^p$  at  $\mathbf{X}_s$  is computed in a similar way. In addition to the penalty forces, other types of forces are exerted at each IB point to simulate locomotion problems. First, to specify the internal elastic property of the swimmer, each IB point is connected by elastic springs to its two neighboring points on the same immersed boundary. Second, each IB point is connected by a stiff spring

to a corresponding “tether” point with imposed track of motion. The movements of the tether point describe the specific gait of swimming.

In addition to the penalty force densities  $\mathbf{F}_n^p$  and  $\mathbf{F}_s^p$ , we denote the densities of other force components (sum of elastic force and tether force) on the two boundaries by  $\mathbf{F}_n^o$  and  $\mathbf{F}_s^o$ . Following the classical IB method, the coupling between the fluids and the immersed boundaries is through the integral relations:

$$\mathbf{f}_j^i(\mathbf{x}, t) = \int_{\Gamma^j} \mathbf{F}_j^i(q, t) \delta(\mathbf{x} - \mathbf{X}_j(q, t)) dq \quad (2.8)$$

$$\frac{\partial \mathbf{X}_j(q, t)}{\partial t} = \int_{\Omega} \mathbf{u}_j(\mathbf{x}, t) \delta(\mathbf{x} - \mathbf{X}_j(q, t)) d\mathbf{x} \quad (2.9)$$

Here  $i = o, p$  and  $j = n, s$ .  $\Omega$  is the fluid domain.  $\mathbf{f}_j^i(\mathbf{x}, t)$  represents the Eulerian force density at  $\mathbf{x}$  contributed by the Lagrangian force  $\mathbf{F}_j^i$ .  $\delta(\mathbf{x}) = \delta(x)\delta(y)$  is the two-dimensional Dirac delta function. Equation (2.8) describes how the Lagrangian forces at each IB point are transmitted to the corresponding fluid phase. Equation (2.9) reflects the fact that each IB object moves with the local fluid velocity. With Eulerian force densities defined above, the force densities in Equations (2.4) and (2.5) are calculated as:

$$\mathbf{f}_n = \theta_n \mathbf{f}_n^o + \theta_n \theta_s \mathbf{f}_n^p, \quad (2.10)$$

and

$$\mathbf{f}_s = \theta_s \mathbf{f}_s^o + \theta_n \theta_s \mathbf{f}_s^p. \quad (2.11)$$

Within each fluid, the Eulerian contributions from  $\mathbf{F}_j^o$  is scaled by the volume fraction of that fluid. On the other hand, the penalty forces are scaled by the product of the volume fractions  $\theta_n \theta_s$  after they are transmitted to each of the fluids. Therefore, no penalty force is generated if either of the volume fractions go to zero. This also ensures that at each location, the total net penalty forces applied to the two fluids

approximately add up to zero, provided that  $\Gamma^n$  and  $\Gamma^s$  are close enough.

## 2.2.2 Model of Finite Swimmer

We extend our study to the investigation of swimmers of finite length. In this model, our primary focus is on the solvent immersed boundary,  $\Gamma^s$ . As shown in Figure 2.3, the swimmer moves in a low-viscosity region, the solvent phase, surrounded by a more viscous bulk fluid, the network phase, with different fluid layers separated by interfaces. Since the swimmer is surrounded by a solvent phase, the forces from the network on the network immersed boundary,  $\Gamma^n$ , are negligible and so do not need to be considered.

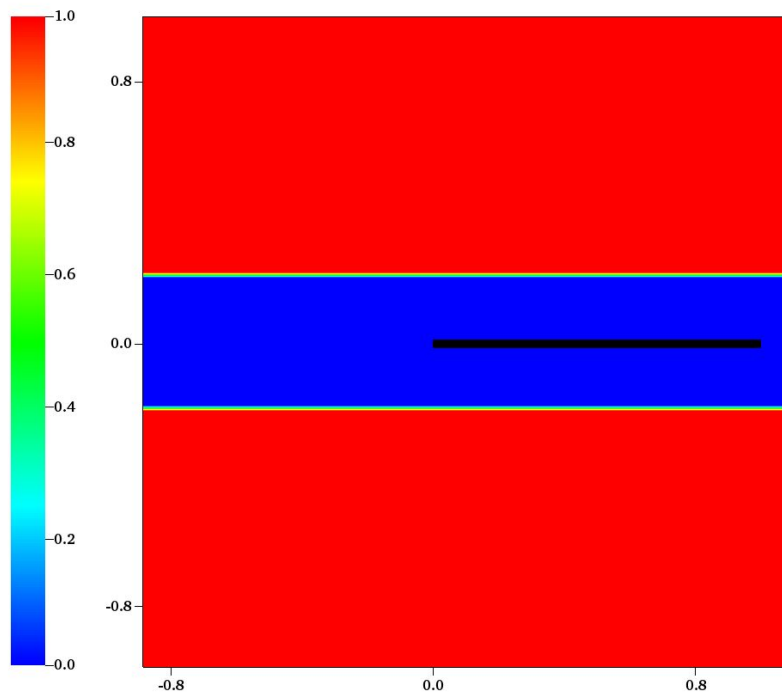


Figure 2.3: Model of Finite Swimmer: The swimmer (represented by the black curve) moves in a low-viscosity region, solvent phase (represented by the blue region), surrounded by a more viscous bulk fluid, network phase (represented by the red region).

The movement of  $\Gamma^s$  is driven using a prescribed target curvature  $\kappa_0(q, t)$  which has the waving form

$$\kappa_0 = Ak^2 \sin(kq + \omega t) \quad (2.12)$$

Both the inextensibility and the shape of the swimmer are enforced by forces that are designed to penalize extension and deviation from the prescribed curvature. A similar model was proposed by [21]. These forces are derived from expressions for the bending energy  $E_b$  and stretching energy  $E_s$  of the swimmer:

$$E_s = \frac{k_s}{2} \int_{\Gamma^s} \left( \left\| \frac{\partial \mathbf{X}_s}{\partial q} \right\| - 1 \right)^2 dq, \quad (2.13)$$

$$E_b = \frac{k_b}{2} \int_{\Gamma^s} (\kappa(q, t) - \kappa_0(q, t))^2 dq. \quad (2.14)$$

Here,  $k_s$  and  $k_b$  are the tensile and bending stiffness of the swimmer, respectively. The elastic force densities on  $\Gamma^s$  are computed using the variation derivative of the total energy:

$$\mathbf{F}_s^e = -\frac{\delta}{\delta \mathbf{X}_s} (E_s + E_b). \quad (2.15)$$

Similar to our previous model, to prevent  $\Gamma^n$  and  $\Gamma^s$  from separating, pairs of corresponding IB points on them is connected by a stiff spring with zero rest length. Penalty forces (with densities of  $\mathbf{F}_s^p$  and  $\mathbf{F}_n^p$ ) are generated at these points when their spatial locations differ. The coupling between the fluids and the immersed boundaries is through the integral relations:

$$\mathbf{f}_j^i(\mathbf{x}, t) = \int_{\Gamma^j} \mathbf{F}_j^i(q, t) \delta(\mathbf{x} - \mathbf{X}_j(q, t)) dq, \quad (2.16)$$

$$\frac{\partial \mathbf{X}_j(q, t)}{\partial t} = \int_{\Omega} \mathbf{u}_j(\mathbf{x}, t) \delta(\mathbf{x} - \mathbf{X}_j(q, t)) dx. \quad (2.17)$$

Here,  $i = e, p$  and  $j = n, s$ . The fluid domain is represented by  $\Omega$ . The Eulerian force density at  $\mathbf{x}$  is represented by  $\mathbf{f}_j^i(\mathbf{x}, t)$ .  $\delta(\mathbf{x}) = \delta(x)\delta(y)$  is the two-dimensional Dirac delta function. Equation (2.18) describes how the Lagrangian forces at each IB point are transmitted to the corresponding fluid phase while equation (2.19) reflects the fact that each IB object moves with the local fluid velocity. Using the Eulerian force densities as defined above, we calculate the force densities as defined in Equations (2.4) and (2.5) as:

$$\mathbf{f}_n = \theta_n \theta_s \mathbf{f}_n^p \quad (2.18)$$

$$\mathbf{f}_s = \theta_s \mathbf{f}_s^e + \theta_n \theta_s \mathbf{f}_s^p. \quad (2.19)$$

## 2.3 Computational Discretization

All fluid variables ( $\mathbf{u}^n, \mathbf{u}^s, p, \theta^n, \theta^s$ ) are discretized using a Cartesian grid, with constant grid space  $h$ . Each immersed boundary object is represented using a discrete set of IB points indexed by the integer  $q$ . Time is discretized into steps of  $\Delta t$ , and the locations of the IB points at time  $t_k = k\Delta t$  are denoted by  $\mathbf{X}^j(q, t_k)$  for  $j = n, s$ . Fluid quantities at an Eulerian grid point  $\mathbf{x}_{lm}$  at this time are identified by  $\mathbf{u}_{lm}^j(t_k)$  and similar expressions. For communication between the Eulerian grid and the IB point locations, we use discrete versions of Equations (2.8)-(2.9). More specifically, we use

$$\mathbf{f}_i^j(\mathbf{x}_{lm}, t_k) = \sum_q \mathbf{F}_i^j(q, t_k) \delta_h(\mathbf{x}_{lm} - \mathbf{X}^j(q, t_k)) \Delta q, \quad (2.20)$$

$$\mathbf{U}^j(\mathbf{X}^j(q, t_k), t_k) = \sum_{l,m} \mathbf{u}_{lm}^j(t_k) \delta_h(\mathbf{x}_{lm} - \mathbf{X}^j(q, t_k)) h^2 \quad (2.21)$$

where  $\delta_h$  is an approximation to the two-dimensional Dirac delta function. In the IB method, this function plays a significant role in the interaction of fluids and bound-

aries. Namely, it is used for the interpolation and spreading of values between these structures. For our work,  $\delta_h$  is defined as

$$\begin{aligned}\delta_h(\mathbf{x}_{lm} - \mathbf{X}^j(q, t_k)) &= \delta_h(x_{lm} - X^j(q, t_k))\delta_h(y_{lm} - Y^j(q, t_k)) \\ &= \frac{1}{h}\phi\left(\frac{x_{lm} - X^j(q, t_k)}{h}\right)\frac{1}{h}\phi\left(\frac{y_{lm} - Y^j(q, t_k)}{h}\right)\end{aligned}\tag{2.22}$$

One key property of this function that guides the spreading of forces in our work is that  $\phi(r) = 0$  for  $|r| \geq 2$ . To satisfy property 2 given above, we need

$$\begin{aligned}&|r| < 2, \\ \implies &\left|\frac{\mathbf{x}_{lm} - \mathbf{X}^j(q, t_k)}{h}\right| < 2 \\ \implies &|\mathbf{x}_{lm} - \mathbf{X}^j(q, t_k)| < 2h\end{aligned}\tag{2.23}$$

This property specifies that the displacement of the spatial locations of the Eulerian fluid points and the Lagrangian points on the immersed boundary must be less than  $2h$  in both the  $x$  and  $y$  direction. These conditions must be met simultaneously to ensure the spread of a non-zero force from the swimmer to the fluid.

The process of the force spreading from the immersed boundary points on the swimmer to the fluid is illustrated in Figures 2.4 and 2.5. In these figures, the red dot represents the location of an arbitrary immersed boundary point on the Lagrangian grid, located at a given cell center, while the green dots represent an arbitrary immersed boundary point on the Lagrangian grid from which the force will be spread. As illustrated in the figures, the location of these green points vary and may be located either to the right or left, and above or below, the cell-centered IB point. The blue arrows, located at the centers of the cell edges on the Eulerian grid, illustrate the location of points on the Eulerian grid to which the forces on the Lagrangian grid are spread (either in the  $x$ -direction or  $y$ -direction). In each case, we obtain a  $4 \times 4$  stencil.

Figure 2.4 illustrates the spreading of forces in the  $x$ -direction. We observe that the support is bounded to a 2-grid shift on each side (left and right) of the immersed boundary point from which the force is being spread. Additionally:

- if the immersed boundary point from which the force is being spread is located below the cell center, the support is bounded by a 2-grid shift below and 1-grid shift above the point.
- if the immersed boundary point from which the force is being spread is located above the cell center, the support is bounded by a 1-grid shift below and 2-grid shift above the point.

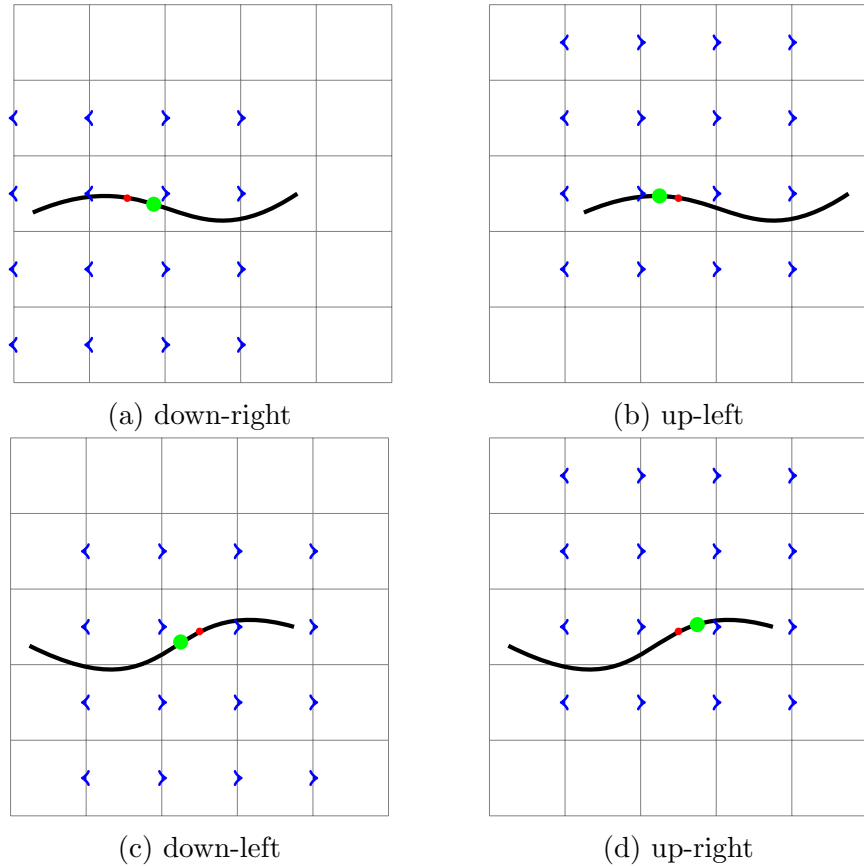


Figure 2.4: Spreading of force in the  $x$ -direction.

Similarly, Figure 2.5 illustrates the spreading of the forces in the  $y$ -direction. Here, we observe that the support is also bounded to a 2-grid shift on each side (above or below) of the immersed boundary point from which the force is being spread. Further:

- if the immersed boundary point from which the force is being spread is located to the right of the cell center, the support is bounded by a 2-grid shift right and 1-grid shift left of the point.
- if the immersed boundary point from which the force is being spread is located to the left of the cell center, the support is bounded by a 1-grid shift right and 2-grid shift left of the point.

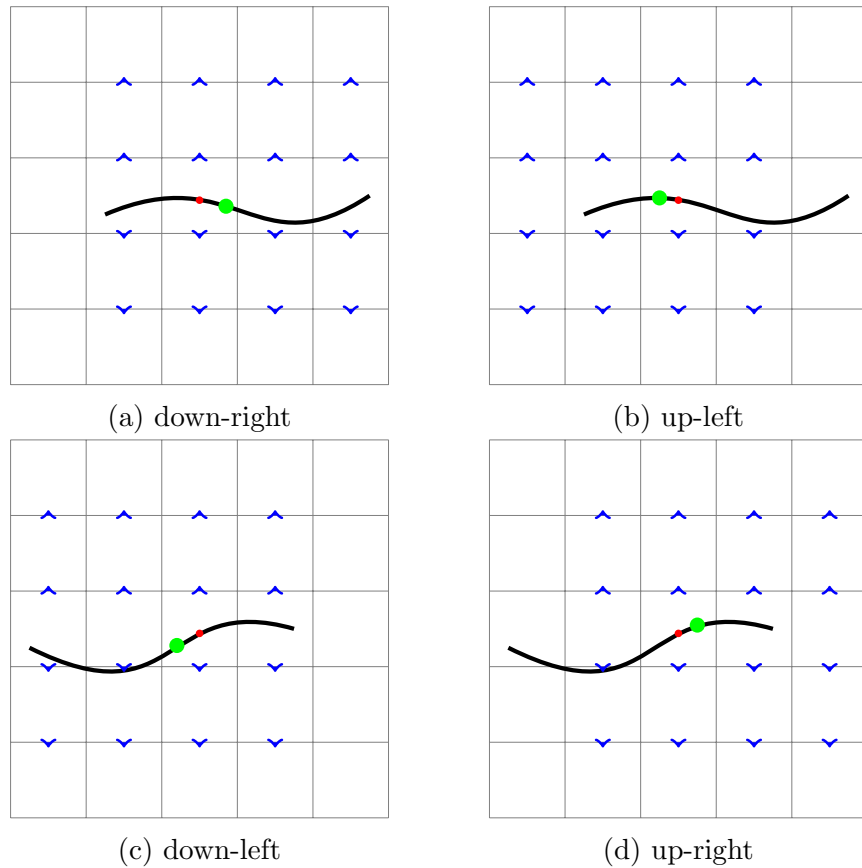


Figure 2.5: Spreading of force in the  $y$ -direction.

Once we determine where to spread the force, we calculate the weights using the Dirac-Delta function. The weights for spreading the  $x$ -force is given as

$$\delta(x) = \begin{cases} \frac{1+\cos(\frac{\pi x}{2h})}{4h}, & x \leq 2h \\ 0, & x > 2h \end{cases} \quad (2.24)$$

and for the  $y$ -force we have

$$\delta(y) = \begin{cases} \frac{1+\cos(\frac{\pi y}{2h})}{4h}, & y \leq 2h \\ 0, & y > 2h \end{cases} \quad (2.25)$$

This spreading process is done for both the solvent and the network.

Once the forces are spread from the Lagrangian grid to the Eulerian grid, we proceed with the interpolation of the fluid velocity to the immersed boundary point (ie. from the Eulerian grid to the Lagrangian grid). To ensure the conservation of energy, the interpolation functions used in both the spreading of forces and the interpolation of fluid velocity, must be the same at each time step. This requires the support (stencil) of any arbitrary immersed boundary point to be identical in both the spreading and interpolation processes. Interpolating the fluid velocity to the immersed boundary point requires essentially the reverse of the spreading process described above. To interpolate the  $x$ -velocity from the fluid to the immersed boundary point, our support, as well as, our weights remain identical to those used for the spreading process. We use the support and weights, in both the  $x$  and  $y$  directions to update the velocity of the immersed boundary points and other immersed boundary sheet points. This interpolation process is done for both the solvent and the network.

A MAC-type staggered computational grid is used for spatial discretization where scalars are located at the grid centers and vectors are located at the grid edges (see Figure 2.6).

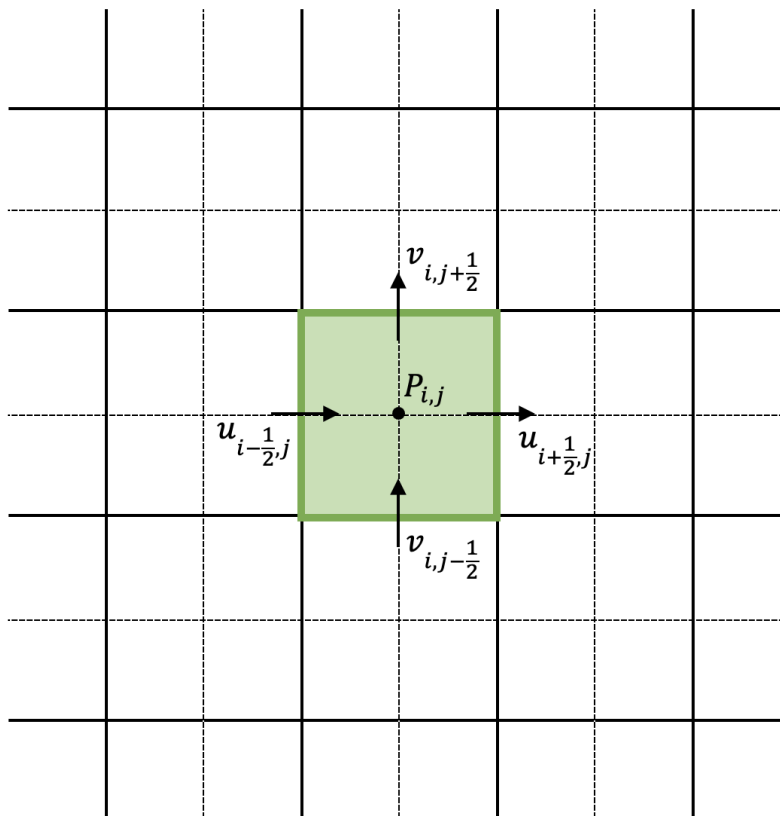


Figure 2.6: MAC-Type Staggered Computational Grid.

## 2.4 Numerical Solutions

We discretize Equations (2.3)-(2.5) as described in detail in [41]. We write the equations in matrix-vector form as:

$$\begin{bmatrix} \mathcal{L}_n - \mathcal{C} & \mathcal{C} & -\mathcal{G}_n \\ \mathcal{C} & \mathcal{L}_s - \mathcal{C} & -\mathcal{G}_s \\ \mathcal{D}_n^T & \mathcal{D}_s^T & 0 \end{bmatrix} \begin{bmatrix} \mathbf{u}^n \\ \mathbf{u}^s \\ p \end{bmatrix} = \begin{bmatrix} \mathbf{f}^n \\ \mathbf{f}^s \\ 0 \end{bmatrix}, \quad (2.26)$$

where

$$\mathcal{L}_{n,s} = \begin{bmatrix} \alpha_{n,s} \partial_x (\theta^{n,s} \partial_x) + \mu_{n,s} \partial_y (\theta^{n,s} \partial_y) & \mu_{n,s} \partial_y (\theta^{n,s} \partial_x) + \lambda_{n,s} \partial_x (\theta^{n,s} \partial_y) \\ \mu_{n,s} \partial_x (\theta^{n,s} \partial_y) + \lambda_{n,s} \partial_y (\theta^{n,s} \partial_x) & \alpha_{n,s} \partial_y (\theta^{n,s} \partial_y) + \mu_{n,s} \partial_x (\theta^{n,s} \partial_x) \end{bmatrix},$$

$$\mathcal{C} = \begin{bmatrix} \xi \theta^n \theta^s & 0 \\ 0 & \xi \theta^n \theta^s \end{bmatrix}, \quad \mathcal{G}_{n,s} = \begin{bmatrix} \theta^{n,s} \partial_x \\ \theta^{n,s} \partial_y \end{bmatrix}, \quad \mathcal{D}_{n,s} = \begin{bmatrix} \partial_x \theta^{n,s} \\ \partial_y \theta^{n,s} \end{bmatrix},$$

$\alpha_{n,s} = (2\mu_{n,s} + \lambda_{n,s})$ .  $\mathbf{f}^j = \theta^j \mathbf{f}_o^j + \theta^n \theta^s \mathbf{f}_p^j$  for  $j = n, s$ . All equations in the above system are discretized using second-order, centered finite differences. When discretized, these equations lead to a large, sparse linear system of saddle point type. A multigrid preconditioned GMRES solver is used to solve the system of equations. The transport equation (2.2) is then solved by the second order corner transport upwind (CTU) scheme as described in [9]. In addition to the discretized version of (2.1)-(2.5), the location of the IB points is updated by:

$$\mathbf{X}_n^{k+1} = \mathbf{X}_n^k + \Delta t S_h^*(\mathbf{u}_n^k), \quad (2.27)$$

$$\mathbf{X}_s^{k+1} = \mathbf{X}_s^k + \Delta t S_h^*(\mathbf{u}_s^k), \quad (2.28)$$

Here the symbol with superscript  $k$  represents the value of the corresponding variable

at time step  $t^k$ .  $S_h^*$  is the discretized version of the interpolation operator as defined in (2.9) and (2.17). The time iteration for the proposed numerical method can be summarized as following:

1. Based on the geometric configuration of IB curves  $\Gamma^n$  and  $\Gamma^s$  at  $t^k$ , compute the total elastic force densities  $\mathbf{F}_n$  and  $\mathbf{F}_s$  on them. Compute the corresponding Eulerian forces  $\mathbf{f}_n^k$  and  $\mathbf{f}_s^k$  by spreading  $\mathbf{F}_n$  to the network and  $\mathbf{F}_s$  to the solvent.
2. Solve discretized versions of (2.3)-(2.5) to get fluid velocities  $\mathbf{u}_n, \mathbf{u}_s$  at  $t^k$ .
3. Update the positions of the IB points at  $t^{k+1}$  according to (2.27) and (2.28).
4. Compute  $\theta_n$  at  $t^{k+1}$  from discretized version of (2.2).
5. Repeat step 1 at next time level  $t^{k+1}$ .

Further details about the computational algorithm are given in [13].

# Chapter 3

## Results

### 3.1 Locomotion of Infinite Swimmer Near Interfaces

#### 3.1.1 Problem Setup

For the model of the swimmer of infinite length, the problem is motivated by the classical Taylor's swimming sheet problem [37]. The swimmer is modeled as an infinite extensible thin sheet, which is a curve in the two dimensional plane. In the reference frame with its swimming speed, the sheet has a waving profile:

$$y = b \sin(kx - \omega t). \quad (3.1)$$

In all 2D plots, the  $x$ -axis and  $y$ -axis are along the horizontal and vertical directions, respectively. We choose  $k = \omega = 2\pi$ . The computational domain is over the rectangular region  $[0, 1] \times [-1.5, 1.5]$ . Periodic boundary conditions are imposed in the  $x$ -direction for all model variables to simulate the movement of an infinite swimmer. No-slip

conditions are imposed for all velocity components at  $y = \pm 1.5$ . The size of the computational grid is  $128 \times 384$ . A constant time step  $\Delta t = 10^{-4}$  is used for all simulations. The swimming sheet is represented by two IB objects ( $\Gamma^n$  and  $\Gamma^s$ ) each with 256 IB points. The swimming speed of the sheet is computed by averaging the  $x$ -velocity of all the IB points over one wave period. We assume a steady value is obtained when the swimming speed varies less than 5% between two consecutive periods.

Since our main focus is to study locomotion within layers of fluid separated by interfaces, we choose the initial profile of the network volume fraction  $\theta_n$  as a piecewise constant function in the  $y$ -direction:

$$\theta_n(x, y, t = 0) = \begin{cases} \theta_n^{\text{in}} & \text{if } |y| \leq H \\ \theta_n^{\text{out}} & \text{if } |y| > H. \end{cases} \quad (3.2)$$

Here, the value of  $H$  defines the initial location of the fluid interface.  $\theta_n^{\text{in}}$  is the network volume fraction in the thin fluid layer in direct contact with the swimmer. This inner layer is surrounded by a bulk fluid with a network volume fraction of  $\theta_n^{\text{out}}$ . Notice that the location of the fluid interfaces may change due to the movement of the swimming sheet. To solve the equations of motion with free boundaries between different phases of materials numerically, interface tracking methods can be used. The location of the interface is followed explicitly, and different PDEs coupled by matching conditions are solved on each side of the interface [40]. In our work, we use an interface capturing strategy [14] in which the same two-fluid Equations (2.3) and (2.4) are solved everywhere throughout the domain. The fluid interface is implicitly represented by the spatial distribution of the volume fraction  $\theta_n$ , which may be regularized numerically to make computational solutions feasible. There is no need to explicitly track the dynamic interface and enforce the interface conditions. Because of the capturing strategy

and numerical smearing, our simulations essentially approximate the fluid interface by a spatial region (in 2D) over which the values of  $\theta_n$  exhibit sharp transitions.

### 3.1.2 Comparison with Analytic Solutions

In this section, we illustrate the accuracy of the numerical algorithm by comparing our simulation results with analytical solutions. In [10, 26], the swimming speed is calculated for an infinite waving sheet in a viscous two-fluid domain, where a low-viscosity fluid layer near the swimmer is surrounded by a more viscous bulk fluid. For reasonable comparisons with asymptotic solutions, we choose  $b = 0.012$  so that  $bk \ll 1$ . As the initial profile, we set  $\theta_n^{\text{in}} = 0$  and  $\theta_n^{\text{out}} = 1$  so that the inner fluid layer only contains a single fluid. Note that the force balance Equations (2.4) and (2.5) become degenerate over the region with  $\theta_s = 0$  or  $\theta_n = 0$ . To avoid this difficulty, we regularize the discrete equations by temporarily adding a small positive constant  $\delta\theta_n = 1.0e - 5$  to  $\theta_n$  throughout the entire domain and solve the same set of two-fluid equations everywhere. The value of  $\theta_s$  is reduced by the same constant to maintain the condition  $\theta_n + \theta_s = 1$ . A large frictional coefficient  $\xi = 10^{10}$  is chosen so that the two velocity fields  $\mathbf{u}_n$  and  $\mathbf{u}_s$  are approximately the same.

### 3.1.3 Swimming Near Non-Deformable Fluid Interface

In [26], the interface between the two fluids remains flat. Across the interface, the component of the fluid velocities is zero. The  $x$ -component of the fluid velocities is continuous. To enforce such interface conditions, we introduced two horizontal IB walls initially located at  $y = \pm H$ . Each wall is composed of two IB objects as described in the previous chapter. To approximate a flat interface during the simulation, every IB point  $(x, y)$  on the walls is connected by a stiff spring to a tether point at  $(x, H)$ .

Penalty forces are generated at IB points on the walls with  $y \neq H$  caused by vertical motions of the fluids. The simulation setup is shown in Figure 3.1. In the plot, the distributions of  $\theta_n$  and  $\mathbf{u}_s$  (as well as  $\mathbf{u}_n$ ) are shown for two simulations with different interface locations at  $t = 0.5$ . The viscosity ratio is set to  $\beta = \frac{\mu_s}{\mu_n} = 0.5$ . The horizontal black lines in the plot are the IB walls that simulate fluid interfaces. The black curves in the middle represent the swimming sheet. For the simulation in which the fluid interfaces are far away from the sheet (Figure 3.1a,  $H = 0.3$ ), the largest fluid velocity (along the  $y$ -direction) appears near the swimmer. The value of  $\|\mathbf{u}_s\|^{\max}$  is close to the largest vertical velocity of the sheet. As shown in Figure 3.1b, the largest fluid velocity appears away from the swimmer along the  $x$ -direction in the simulation with  $H = 0.16$ . Due to the confinement effect from the flat interfaces, the counter-rotating vortices are much stronger for the simulation with smaller  $H$ . The net effect is that the waving sheet closer to the interfaces tends to move faster along the negative  $x$ -axis.

In Figure 3.2a,b, the simulated swimming speed (scaled by the swimming speed in a single phase Newtonian fluid  $U_0$ ) is plotted as a function of the nondimensional interface height  $kH$  for two sets of simulations with viscosity ratios  $\beta = 0.5$  and  $\beta = 0.1$ , respectively. For a fixed value of  $kH$ , the sheet swims faster with more significant viscosity differences between the two fluid layers. The simulations agree well with the 2nd order analytic results in [26]. In Table 3.1, the relative errors for the results of our simulations compared with the results of the analytical solutions are shown for  $\beta = 0.5$  and  $\beta = 0.1$  and different nondimensional interface height  $kH$ . The relative errors increase slightly with the increase of  $\beta$ .

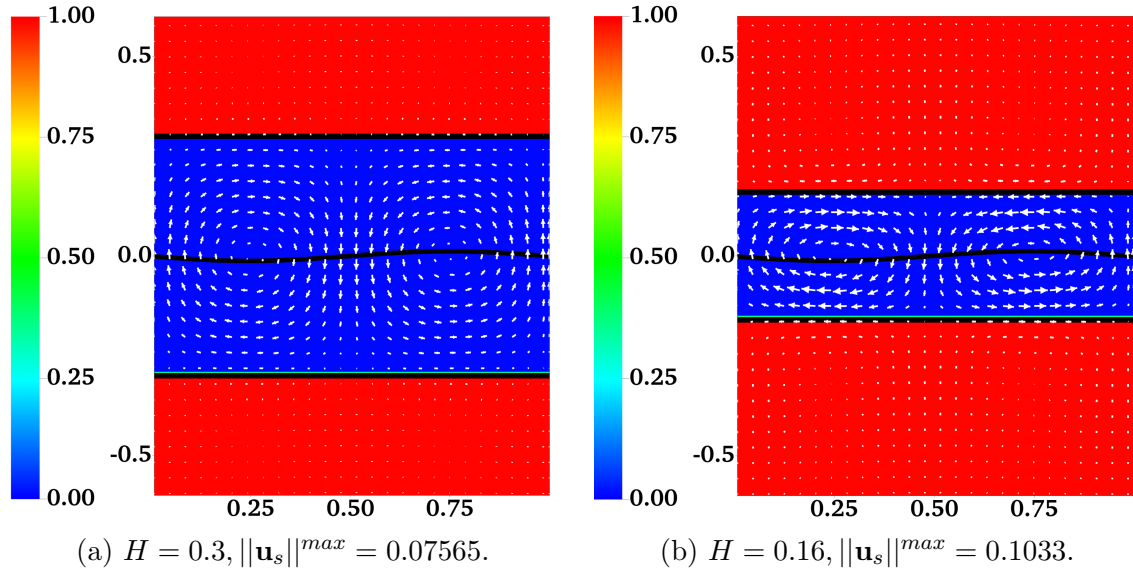


Figure 3.1: Distribution of network volume fraction  $\theta_n$  and fluid velocity  $\mathbf{u}_s$  at  $t = 0.5$  for different  $H$ . All vectors have the same scale. The viscosity ratio between the two fluids is  $\beta = 0.5$ .

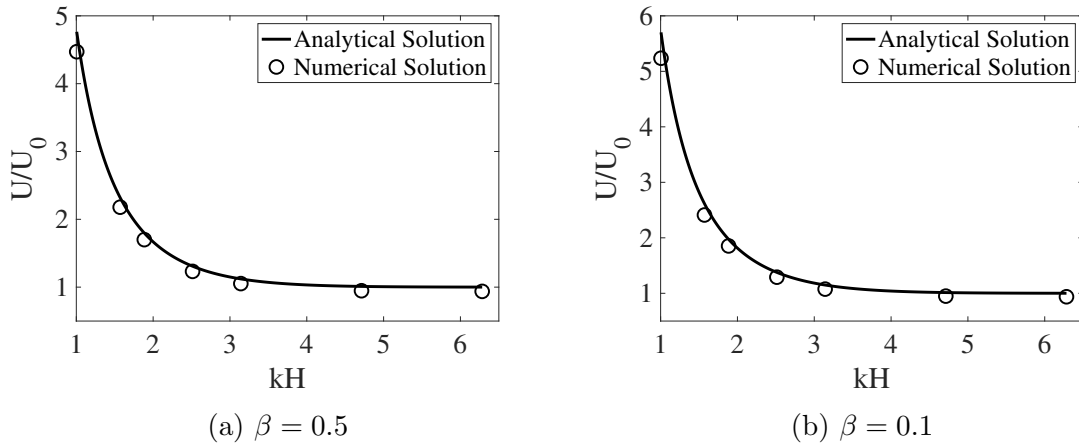


Figure 3.2: The scaled swimming speed vs. the nondimensional interface height  $kH$  for different  $\beta$ . The fluid interfaces are non-deformable. The analytical solutions are from [26].

Table 3.1: Relative errors of the simulated swimming speed for different  $\beta$  and nondimensional interface height  $kH$ . The fluid interfaces are non-deformable. The analytical solutions are from [26].

<b>Relative Error</b>		
<b><math>kH</math></b>	<b><math>\beta = 0.5</math></b>	<b><math>\beta = 0.1</math></b>
$0.32\pi$	6.3%	7.5%
$0.5\pi$	6.0%	7.8%
$0.6\pi$	5.6%	6.1%
$0.8\pi$	5.3%	5.8%
$\pi$	6.2%	6.0%
$1.5\pi$	5.9%	5.9%
$2\pi$	6.0%	6.2%

### 3.1.4 Swimming Near Deformable Fluid Interface

The assumption that the fluid interfaces remain flat near a waving sheet is only valid for large  $H$  or small  $\beta$ . In [10], the locomotion of an infinite swimmer close to a deformable interface between two viscous fluids is investigated analytically. The interface condition is given by the continuity of stress and velocity. To illustrate the accuracy of our interface-capturing scheme, we remove the IB walls at  $y = \pm H$  and redo the simulations as described in the previous section. In Figures 3.3 and 3.4, the distributions of  $\theta_n$  and  $\mathbf{u}_s$  are plotted for simulations with  $\beta = 0.5$  and  $\beta = 0.1$ , respectively. As an indication of the interface locations, the jump in  $\theta_n$  is slightly smeared over 1 – 2 mesh blocks at  $t = 0.5$  relative to its initial sharp profile. The interfaces deform from their horizontal configurations due to the waving motion of the swimmer. For interfaces closer to the swimmer, the deformations are more significant. Comparing Figure 3.4 with Figure 3.3, there are less interface deformations in the simulation with a smaller viscosity ratio  $\beta$ . Because of the smearing effect, we choose to visualize the fluid interfaces using the countour lines of  $\theta_n = 0.5$ , a value in the middle of the network volume fractions within the inner and outer layers of fluids. The swimming sheet, the “fluid interfaces”,

and the fluid velocity are plotted in Figure 3.5 for two simulations with  $\beta = 0.5$  and  $\beta = 0.1$  at different times. The initial swimmer-interface distance is  $H = 0.16$ . It can be noticed that for the simulation with a smaller viscosity ratio (right column of Figure 3.5), the less deformed fluid interfaces provide more effective confinements to the swimmer. Thus, the fluid velocity exhibits stronger counter-rotating vortices than those in the simulation with a larger  $\beta$  (left column of Figure 3.5). By the time at  $t = 1.0$  (which is exactly one wave period), all fluid interfaces return approximately back to their initial horizontal positions.

In Figure 3.6, the simulated swimming speed is compared with the 2nd order analytical result in [10]. The agreement is very good. In Table 3.2, the relative errors for the results of our simulations compared with the results of the analytical solutions are shown for  $\beta = 0.5$  and  $\beta = 0.1$  and different nondimensional interface height  $kH$ . Based on the computed relative errors, we observe that generally, as the value of  $\beta$  decreases, the relative errors increase. We also observe for both  $\beta = 0.5$  and  $\beta = 0.1$ , the relative error for the deformable interface is significantly less than that of the non-deformable interface.

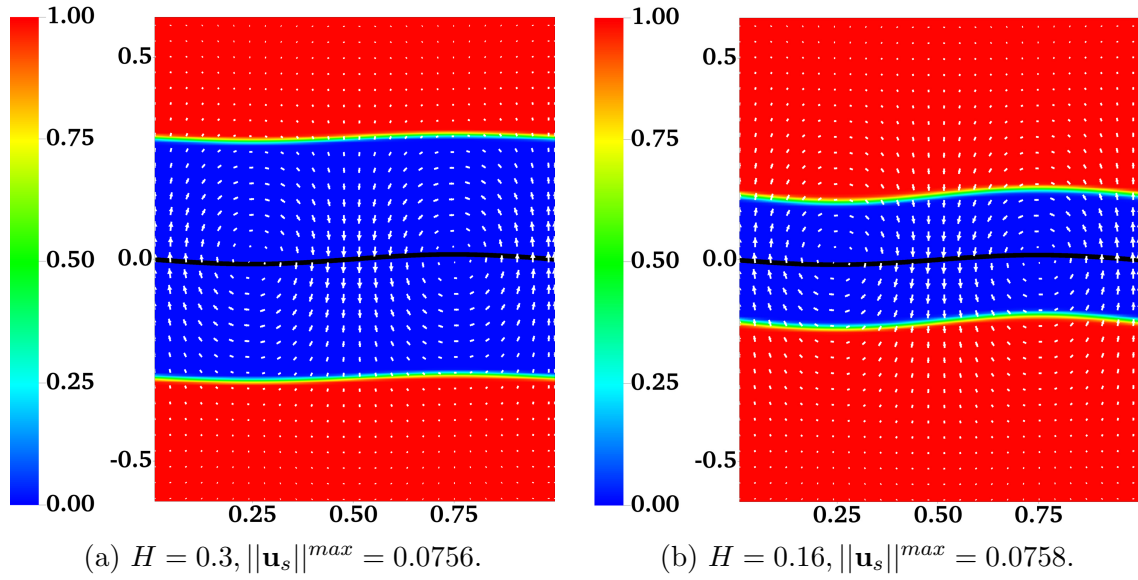


Figure 3.3: Distribution of network volume fraction  $\theta_n$  and fluid velocity  $\mathbf{u}_s$  at  $t = 0.5$  for different  $H$ . All vectors have the same scale. The viscosity ratio between the two fluids is  $\beta = 0.5$ .

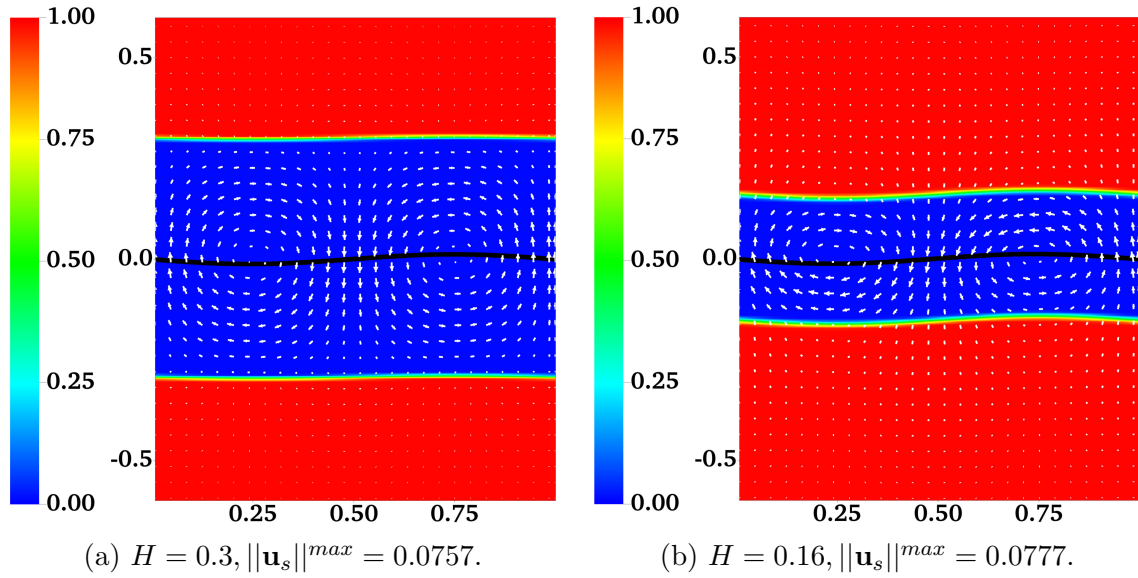


Figure 3.4: Distribution of network volume fraction  $\theta_n$  and fluid velocity  $\mathbf{u}_s$  at  $t = 0.5$  for different  $H$ . All vectors have the same scale. The viscosity ratio between the two fluids is  $\beta = 0.1$ .

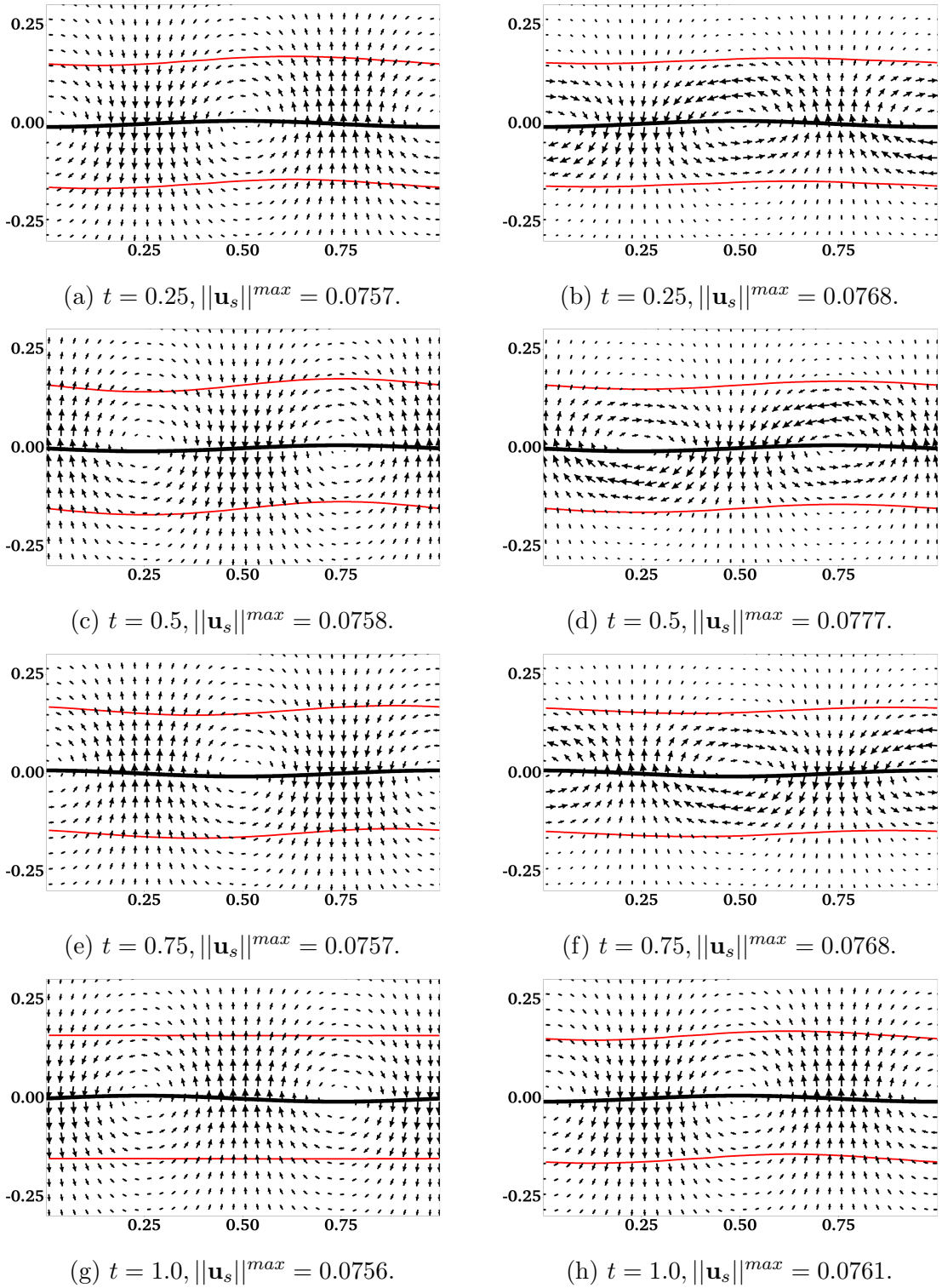


Figure 3.5:  $H = 0.16$ . Distributions of  $\mathbf{u}_s$ , the profiles of swimming sheet (black curves) and fluid interfaces (red curves) for different  $\beta$ . (a,c,e,g) are for  $\beta = 0.5$ . (b,d,f,h) are for  $\beta = 0.1$ . All vectors have the same scale.

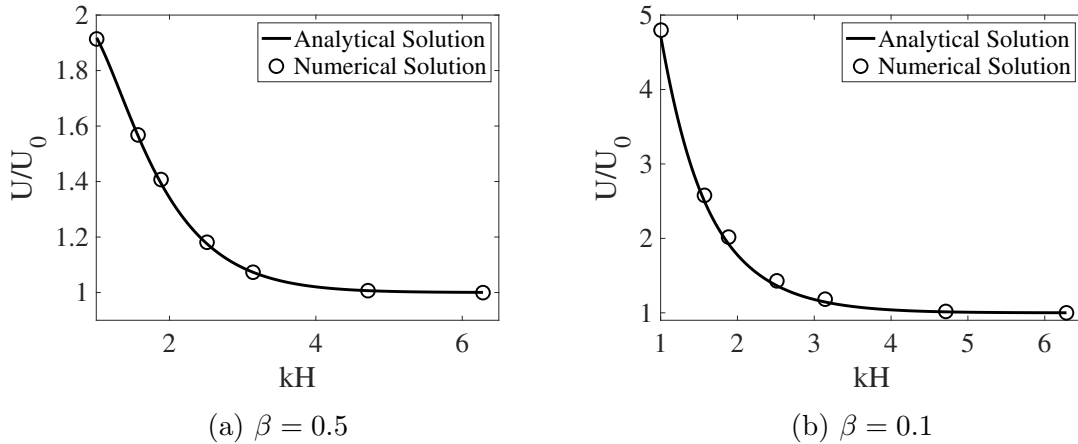


Figure 3.6: The scaled swimming speed vs. the nondimensional interface height  $kH$  for different  $\beta$ . The fluid interfaces are deformable. The analytical solutions are from [10].

Table 3.2: Relative errors of the simulated swimming speed for different  $\beta$  and nondimensional interface height  $kH$ . The fluid interfaces are deformable. The analytical solutions are from [10].

<b>Relative Error</b>		
<b><math>kH</math></b>	<b><math>\beta = 0.5</math></b>	<b><math>\beta = 0.1</math></b>
$0.32\pi$	0.20%	2.1%
$0.5\pi$	0.19%	3.2%
$0.6\pi$	1.0%	4.8%
$0.8\pi$	0.43%	4.8%
$\pi$	0.01%	3.5%
$1.5\pi$	0.01%	0.6%
$2\pi$	0.03%	0.2%

### 3.1.5 Force Analysis

For a Stokes swimmer, the swimming speed is determined by a balance of thrust and drag forces [23]. Here the thrust  $F_T$  is defined as the anchoring force applied so that the undulating sheet is prevented from swimming. The drag is the force  $F_D$  required to tow the sheet with a frozen shape at the swimming speed  $U$ . Due to linearity of Stokes

flow, the drag force can be expressed as  $F_D(U) = \gamma U$ , where the magnitude of the drag coefficient  $\gamma$  is equal to  $F_D(1)$ . To compute the thrust force, we carry out simulations in which tether points are used to prevent IB points on a waving sheet from moving in the  $x$  direction.  $F_T$  is computed as the total tethering force on the sheet, averaged over one wave period. Similarly, for simulations in which IB points on a frozen sheet are connected to tether points moving with velocity of 1 along the  $x$  direction,  $\gamma$  can be calculated from the time averaged towing force on the sheet. From the force balance equation  $F_T + F_D = 0$ , the swimming speed is given by  $U = -\frac{F_T}{\gamma}$ . To confirm the accuracy of the thrust and drag calculation from the simulations, we list the simulated results in Tables 3.3 and 3.4 for non-deformable and deformable interfaces, respectively. The viscosity ratio is  $\beta = 0.5$  for all calculations. As seen from the tables, the ratio between the thrust force and the drag coefficient from the simulations is very close to the swimming speed of the sheet.

Table 3.3: Non-deformable interface ( $\beta = 0.5$ ): thrust force, drag coefficient, their ratio, and the simulated swimming speed.

<b>kH</b>	<b>Thrust Force (<math>F_T</math>)</b>	<b>Drag Coefficient (<math>\gamma</math>)</b>	$-\frac{F_T}{\gamma}$	<b>Swimming Speed U</b>
0.16	$3.03 \times 10^{-2}$	$2.43 \times 10^{-1}$	$-1.247 \times 10^{-1}$	$-1.262 \times 10^{-1}$
0.25	$1.41 \times 10^{-2}$	$2.3 \times 10^{-1}$	$-6.130 \times 10^{-2}$	$-6.151 \times 10^{-2}$
0.4	$7.36 \times 10^{-3}$	$2.12 \times 10^{-1}$	$-3.472 \times 10^{-2}$	$-3.479 \times 10^{-2}$

Table 3.4: Deformable interface ( $\beta = 0.5$ ): thrust force, drag coefficient, their ratio, and the simulated swimming speed.

<b>kH</b>	<b>Thrust Force (<math>F_T</math>)</b>	<b>Drag Coefficient (<math>\gamma</math>)</b>	$-\frac{F_T}{\gamma}$	<b>Swimming Speed U</b>
0.16	$1.23 \times 10^{-2}$	$2.43 \times 10^{-1}$	$-5.062 \times 10^{-2}$	$-5.073 \times 10^{-2}$
0.25	$9.54 \times 10^{-3}$	$2.3 \times 10^{-1}$	$-4.147 \times 10^{-2}$	$-4.151 \times 10^{-2}$
0.4	$6.63 \times 10^{-3}$	$2.12 \times 10^{-1}$	$-3.127 \times 10^{-2}$	$-3.124 \times 10^{-2}$

In Figure 3.7, we plot the thrust force and the drag coefficient for different values of  $kH$  from the simulations with non-deformable interfaces. Both  $F_T$  and  $\gamma$  increase as the fluid interfaces get closer to the swimmer. The variation is approximately linear for  $\gamma$  and superlinear for  $F_T$ . As a result, swimmers near non-deformable fluid interfaces always move faster than those in a single fluid, as observed in Figure 3.2. The enhancement of the swimming speed is more dramatic at smaller values of  $kH$ , where the thrust force increases more significantly. For simulations in which the interfaces are deformable, the value of  $F_T$  and  $\gamma$  are plotted in Figure 3.8 for  $\beta = 0.5$  and  $0.1$ . Comparing Figure 3.8a,b with Figure 3.7, we see that for a fixed viscosity ratio, the drag coefficient is almost identical for simulations with non-deformable and deformable interfaces. On the other hand, close to  $kH = 1$ , the thrust force is much smaller in the simulations with deforming interfaces. Physically, a swimmer can move much faster near non-deformable interfaces than near deformable ones, due to the larger thrust force from the stronger confinement effect. Comparing the thrust and drag curves for different values of  $\beta$  in Figure 3.8, it is noticed that for the same value of  $kH$ , both  $F_T$  and  $\gamma$  increase with the decrease of  $\beta$ . Compared with the drag coefficient, the rate of increase is higher for the thrust force. As a result, the sheet can move faster within two fluid layers where there is a greater viscosity difference.

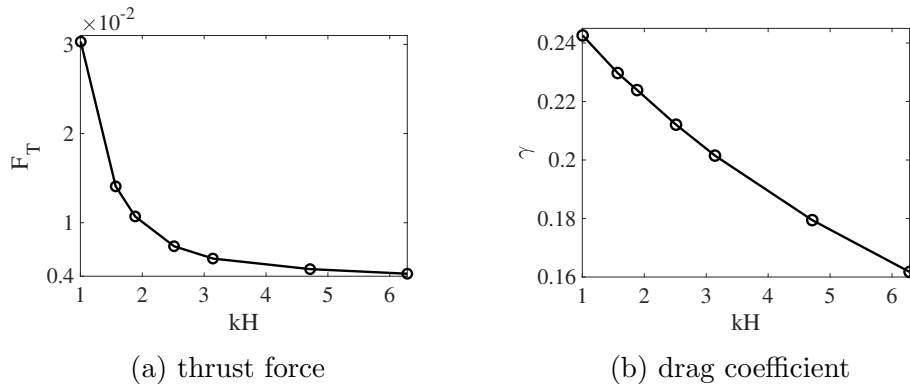
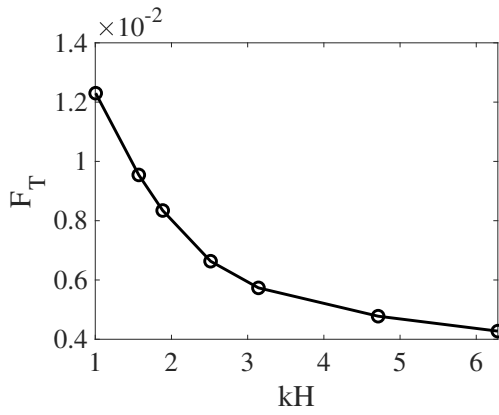
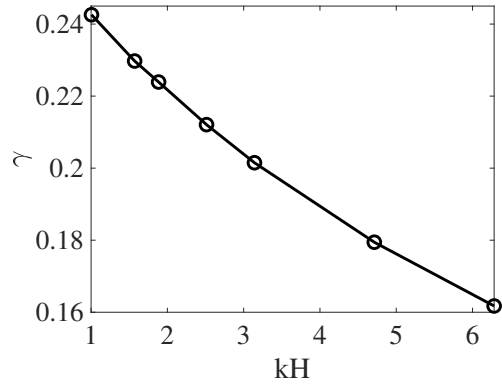


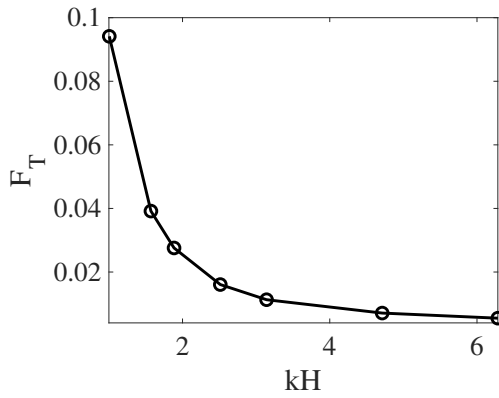
Figure 3.7: Thrust and drag coefficient vs. the nondimensional interface height  $kH$ .  $\beta = 0.5$ . The fluid interfaces are not deformable.



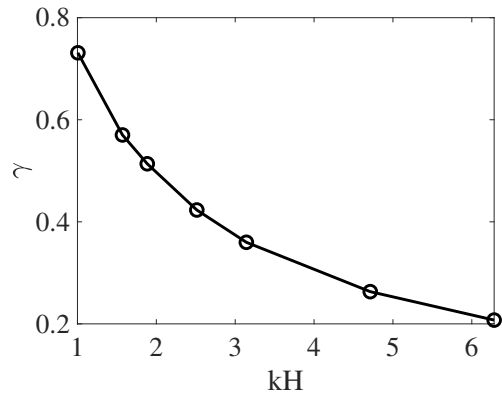
(a) thrust force,  $\beta = 0.5$ .



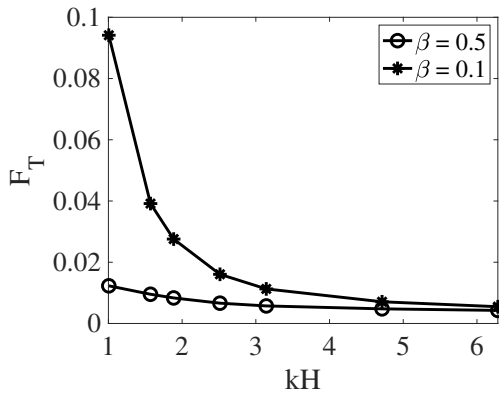
(b) drag coefficient,  $\beta = 0.5$ .



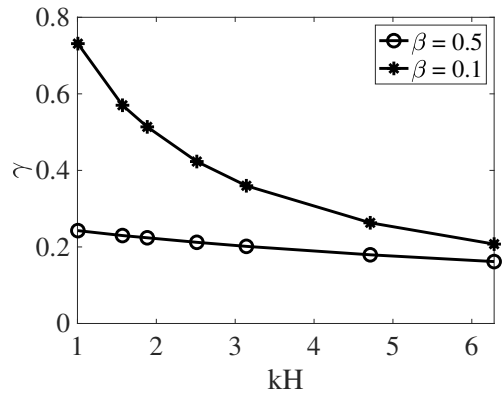
(c) thrust force,  $\beta = 0.1$ .



(d) drag coefficient,  $\beta = 0.1$ .



(e) thrust force,  $\beta = 0.1$  vs.  $\beta = 0.5$ .



(f) drag coefficient,  $\beta = 0.1$  vs.  $\beta = 0.5$ .

Figure 3.8: Thrust and drag coefficient vs. the nondimensional interface height  $kH$  for different  $\beta$ . The fluid interfaces are deformable.

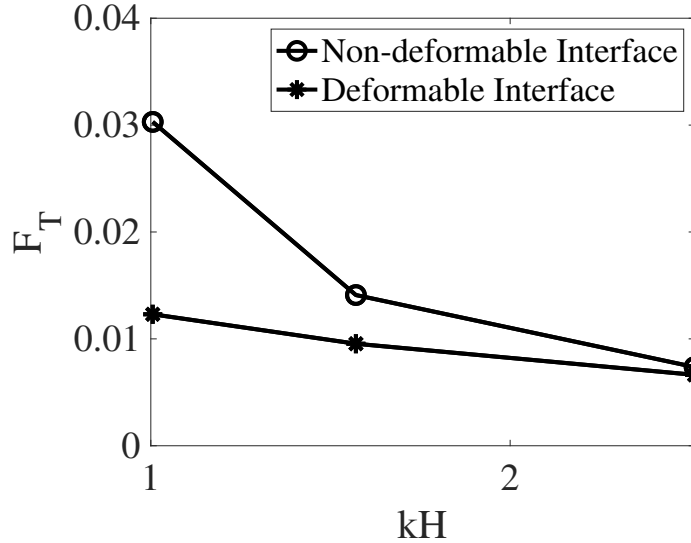


Figure 3.9: Comparison of the effect of interface rigidity: Thrust force vs. the nondimensional interface height  $kH$  for non-deformable vs. deformable interface.  $\beta = 0.5$ .

Although the drag coefficient shows little sensitivity to interface rigidity, as evident in Figures 3.7b and 3.8b, the thrust force varies depending on the rigidity. Figure 3.9 illustrates this effect. Notably, we observe an increase in thrust force for non-deformable interfaces compared to deformable interfaces.

### 3.1.6 Swimming Near Deformable Interface in Fluid Mixtures

For all simulations presented so far, the continuum medium on each side of the interface is modeled as a single phase viscous fluid. Such models may not be suitable for some applications. For example, many biological fluids such as gastric mucus are mixtures composed of a polymer network immersed in a fluid solvent. The mixture can not be adequately described as a single phase homogeneous medium if the composition of the mixture has large spatial variations, or when there is significant relative motions between different components in the mixture. In this section, we investigate problems for which analytical solutions are not available. Specifically, we study the dynamics of

the swimming sheet in mixtures of fluid separated by free interfaces. The main focus is on the effect of fluid composition and frictional drag on the swimming motion. A relatively large wave amplitude  $b = 0.048$  is chosen for the swimming sheet. At the initial time, the network volume fraction in the bulk fluid away from the swimmer is set to  $\theta_n^{\text{out}} = 0.8$ . The values of  $\theta_n^{\text{in}}$  for the mixture around the swimmer is varied between simulations. We also vary the frictional coefficient,  $\xi$ , between the network and the solvent to investigate the influence of phase separation on locomotion. For all simulations in this section, the viscosity ratio between the solvent and the network is  $\beta = 0.25$ .

In Figure 3.10, the distributions of  $\theta_n$  and  $\mathbf{u}_n$  are plotted at different times for the simulation in which  $H = 0.16$ ,  $\xi = 100$ , and  $\theta_n^{\text{in}}$  is set to 0.2 at the initial time. To give a better contrast, white color is used to fill regions with  $\theta_n > \theta_n^{\text{in,max}}$ , where  $\theta_n^{\text{in,max}} = 0.26$  is the largest value of  $\theta_n$  observed near the sheet during the simulation. In Figure 3.10 (b)–(e), the boundaries of the colored region (contour lines of  $\theta_n = \theta_n^{\text{in,max}}$ ) are referred to as the "fluid interfaces". As time progresses, spatial inhomogeneities in  $\theta_n$  and deformations of fluid interfaces appear with the waving motion of the sheet. Compared with the plots at  $t = 0.25$  and  $t = 0.75$ , there are more significant inhomogeneities in the spatial distribution of  $\theta_n$  at the half wave period  $t = 0.5$ . Interestingly, it is also at  $t = 0.5$  that the fluid interfaces and the swimmer have approximately the same phase. At one wave period  $t = 1.0$ , the distribution of network volume fraction roughly returns to its initial value of 0.2 over the entire inner layer. At  $t = 1.0$ , although the fluid interfaces do not fully return to their horizontal positions, their vertical deformations are the smallest within the wave period. Relative to the results at earlier time, the network velocity,  $\mathbf{u}_n$ , tends to have smaller x-components at  $t = 1.0$ . The distributions of  $\theta_n$  over the outer layers of fluid and the solvent velocity,  $\mathbf{u}_s$ , are plotted in Figure 3.11. Here white color is used to fill the region where  $\theta_n > \theta_n^{\text{in,out}}$ , with  $\theta_n^{\text{in,out}} = 0.72$  being

approximately the smallest value of  $\theta_n$  in the outer layer. The fluid interfaces and  $\theta_n$  in the plot exhibit similar periodic patterns in time as observed in Figure 3.10. Notice that due to the numerical smearing, there is a small vertical displacement (about 2 grid blocks) between the fluid interfaces visualized in Figures 3.10 and 3.11. At one wave period  $t = 1.0$ , x-components of the solvent velocity have smaller magnitude than those at an earlier time. Due to its low viscosity, the solvent has greater motion than the network in the vicinity of the swimmer.

In Figure 3.12, we plot the distributions of  $\theta_n$  and the velocity difference  $\mathbf{u}_n - \mathbf{u}_s$  for two simulations with  $\xi = 100$  and  $\xi = 1000$ , at  $t = 0.5$ . With a 10-fold increase of the frictional coefficient, there is a drastic reduction in both the extent of phase separation and the relative motion between the two fluids. The region with the largest velocity difference is near the fluid interfaces. A close look at the plot indicates that the interface deformation is larger than in the simulation with a larger frictional coefficient (not shown). In Figure 3.13, we show the distributions of  $\theta_n$  and  $\mathbf{u}_s$  from two simulations with  $H = 0.32$  and  $H = 0.5$  at  $t = 0.5$  and  $t = 1$ . Regions with  $\theta_n > 0.25$  are filled with white color. Comparing the plots in Figure 3.13a,b, we see that with the locations of the fluid interfaces further away from the swimmer, both the interface deformation and the extent of phase separation are reduced. The vortices of  $\mathbf{u}_s$  for the simulation with  $H = 0.32$  are stronger than those in the simulation with  $H = 0.5$ . As indicated in Figure 3.13c,d, at one wave period  $t = 1$ , the distributions of  $\theta_n$  return approximately to their initial profile for both simulations. Furthermore, at this moment, all fluid interfaces are horizontal approximately, especially for the simulation with the larger value of  $H$ .

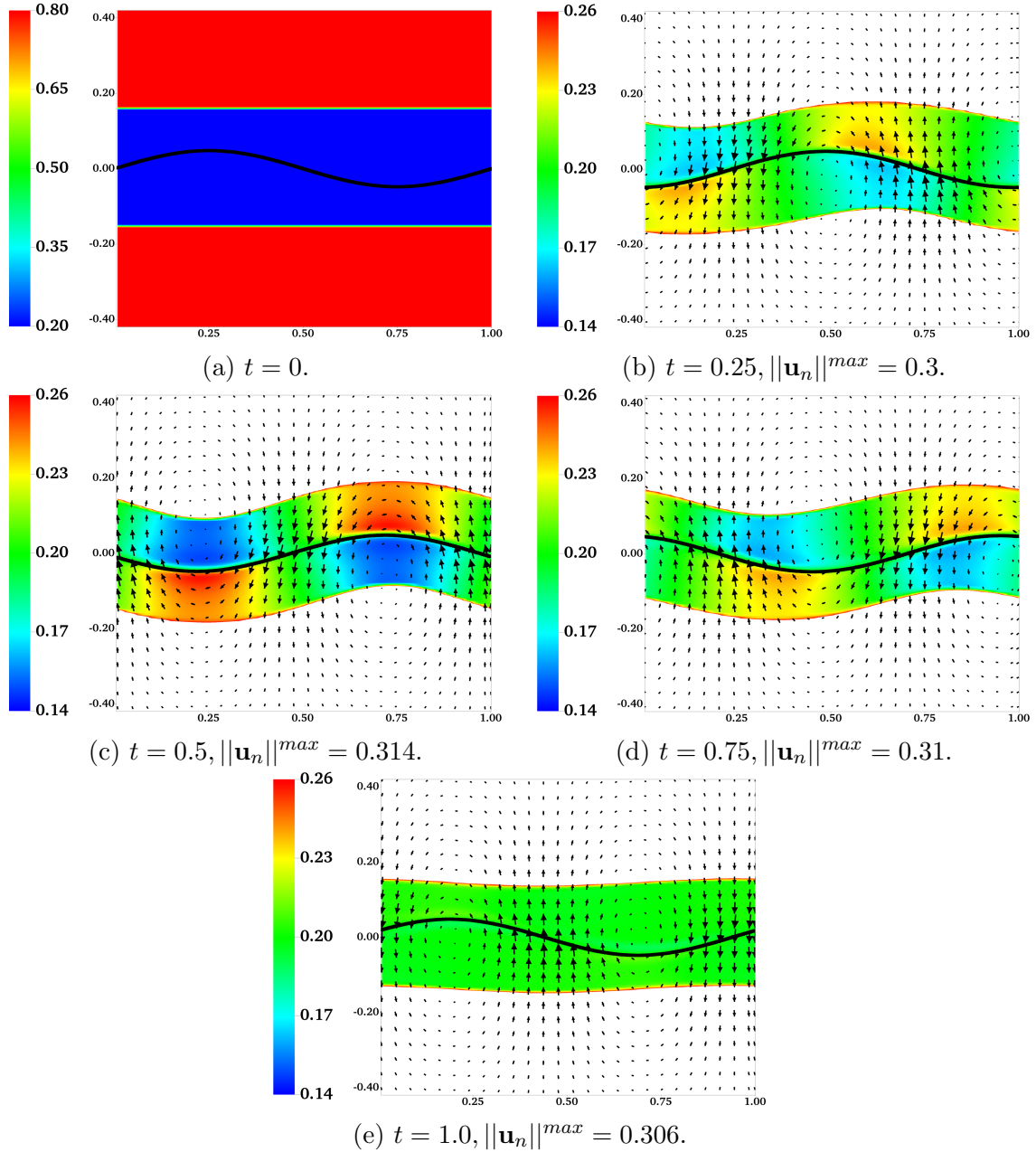


Figure 3.10:  $H = 0.16$ ,  $\beta = 0.25$ ,  $\xi = 100$ ,  $\theta_n^{in} = 0.2$ , and  $\theta_n^{out} = 0.8$ . Distributions of  $\theta_n$  and  $\mathbf{u}_n$  at different times. All vectors have the same scale.

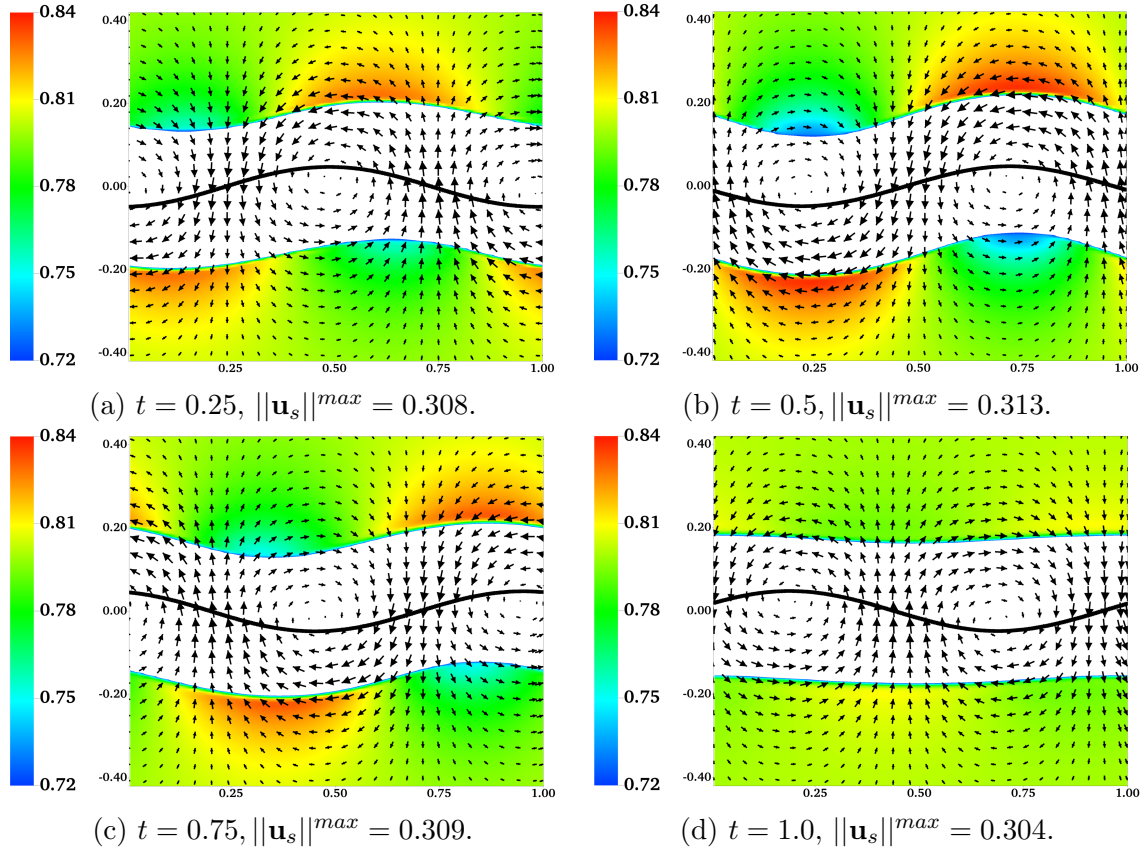


Figure 3.11:  $H = 0.16$ ,  $\beta = 0.25$ ,  $\xi = 100$ ,  $\theta_n^{in} = 0.2$ , and  $\theta_n^{out} = 0.8$ . Distributions of  $\theta_n$  and  $\mathbf{u}_s$  at different times. All vectors have the same scale.

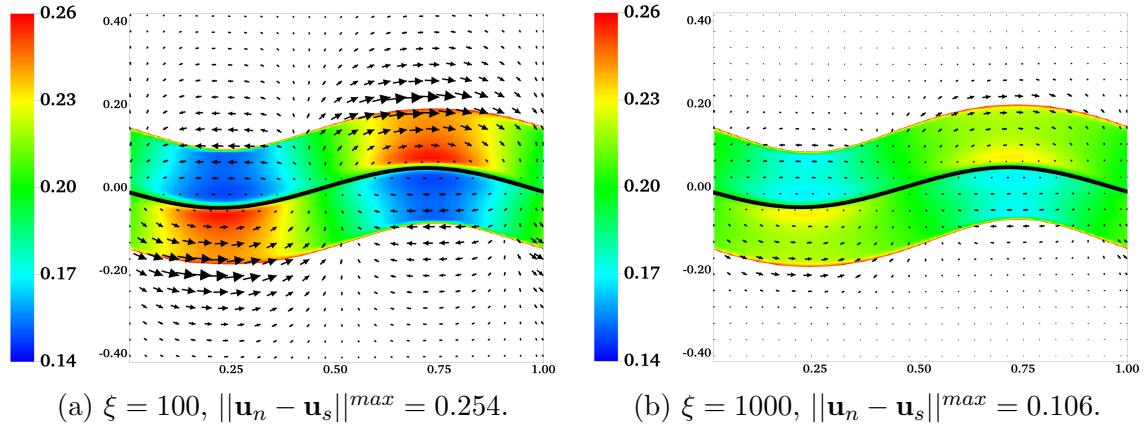


Figure 3.12: Effect of frictional coefficient:  $H = 0.16$ ,  $\beta = 0.25$ ,  $\theta_n^{in} = 0.2$ , and  $\theta_n^{out} = 0.8$ . Distributions of  $\theta_n$  and velocity difference  $\mathbf{u}_n - \mathbf{u}_s$  at  $t = 1.0$ . All vectors have the same scale.

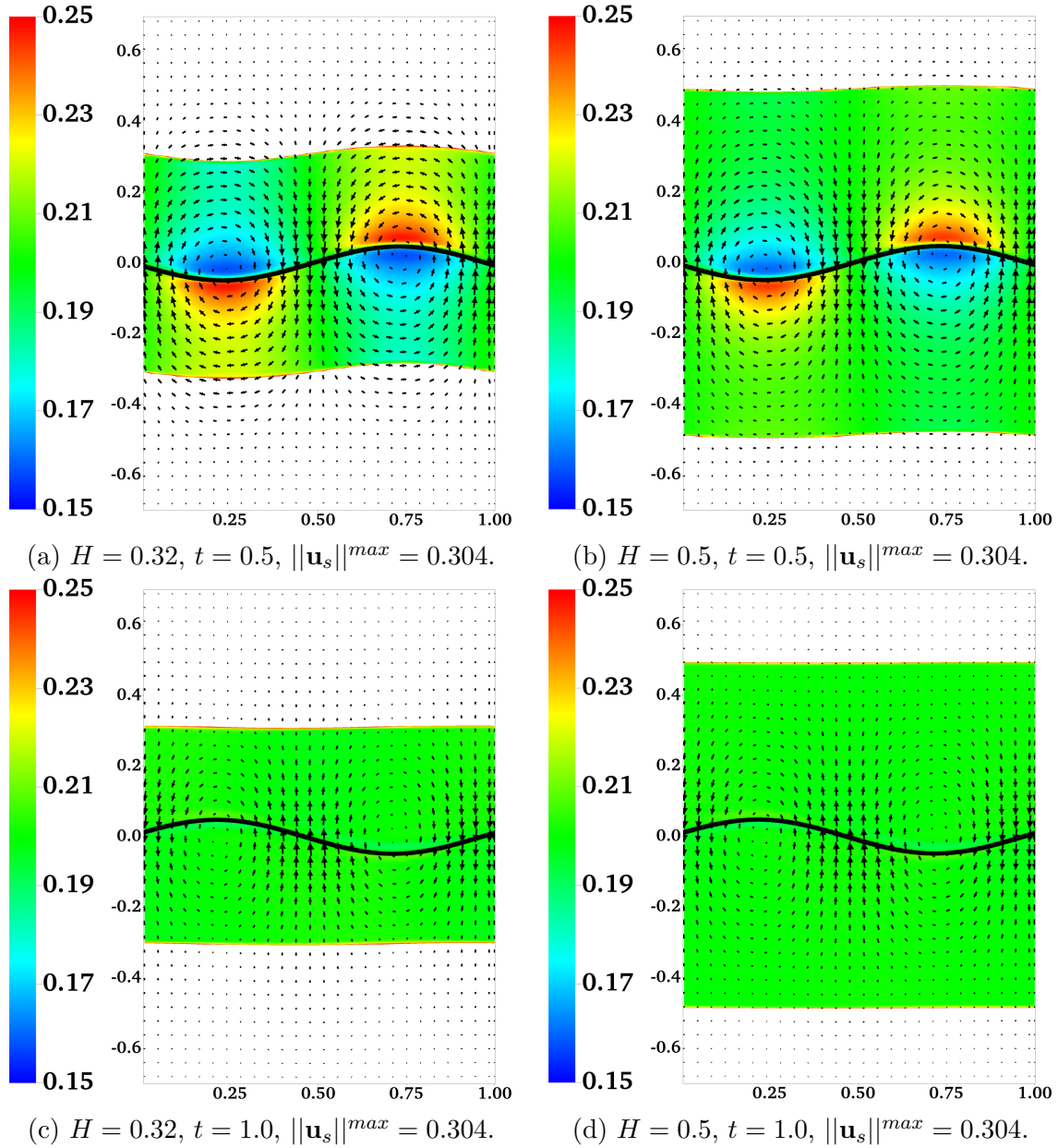


Figure 3.13: Effect of interface location  $H$ :  $\beta = 0.25, \xi = 100, \theta_n^{in} = 0.2,$  and  $\theta_n^{out} = 0.8.$  Distributions of  $\theta_n$  and  $\mathbf{u}_s$  at different times. All vectors have the same scale.

In Figure 3.14, the scaled swimming speed  $\frac{U}{U_0}$  is plotted as a function of the network volume fraction  $\theta_n^{in}$  for  $H = 0.5, H = 0.32,$  and  $H = 0.16.$  The value of  $\theta_n^{out}$  is 0.8 for all simulations. For all values of  $H,$  the swimming speed always increases with the increase of the frictional coefficient for a given  $\theta_n^{in}.$  This is consistent with the

conclusion from [15], in which the swimming sheet problem is investigated in a two-fluid mixture without interfaces. In the simulations with the largest drag of  $\xi = 10^5$ , the network and the solvent move approximately with the same velocity. Therefore, the inner fluid layer behaves like a single phase fluid with the effective viscosity of  $\mu_{\text{eff}}^{\text{in}} = \theta_n^{\text{in}} \mu_n + (1 - \theta_n^{\text{in}}) \mu_s$ . Similarly, the effective viscosity of the outer layer is given by  $\mu_{\text{eff}}^{\text{out}} = \theta_n^{\text{out}} \mu_n + (1 - \theta_n^{\text{out}}) \mu_s$ . Based on the viscosity ratio  $\beta = \frac{\mu_{\text{eff}}^{\text{in}}}{\mu_{\text{eff}}^{\text{out}}}$ , we can use the analytical formula from [10] to compute the swimming speed. The results are plotted as the solid black curves in Figure 3.14. Despite the relatively large amplitude of the waving sheet and large interface deformations, the simulation results agree very well with the analytical solutions. Notice that for the simulations with the largest drag, the swimming speed in a single phase fluid is recovered ( $\frac{U}{U_0} \approx 1$ ) when  $\theta_n^{\text{in}} = \theta_n^{\text{out}} = 0.8$ . For all other values of  $\theta_n^{\text{in}} < 0.8$ , the sheet always swims faster than that in a single fluid, due to the confinement effect from the interfaces.

In the simulations with  $\xi = 10^2$  and  $\xi = 10^3$ , the relations between the swimming speed and  $\theta_n^{\text{in}}$  exhibit different trends depending on the value of  $H$ . When the fluid interfaces are close to the swimmer ( $H = 0.16$ ), the swimming speed always decreases with the increase of  $\theta_n^{\text{in}}$ . This is illustrated in Figure 3.14a. The increase of the network volume fraction near the swimmer reduces the viscosity difference between the inner and outer fluid layers. This tends to weaken the confinement effect of the interfaces and reduce the swimming speed. For some values of  $\theta_n^{\text{in}}$ , the scaled swimming speed is less than one. For a much larger swimmer-interface distance  $H = 0.32$  (Figure 3.14b), the swimming speed in the simulations with intermediate frictional coefficient of  $\xi = 10^3$  still goes down as the values of  $\theta_n^{\text{in}}$  increase. The swimming speed  $U$  is less than  $U_0$  if the value of  $\theta_n^{\text{in}}$  is close to 0.8. By contrast, a non-monotone dependence of the swimming speed on  $\theta_n^{\text{in}}$  is observed for the simulation with  $\xi = 10^2$ . In this case, the ratio of  $\frac{U}{U_0}$  is always less than one. With interfaces further away from the swimmer

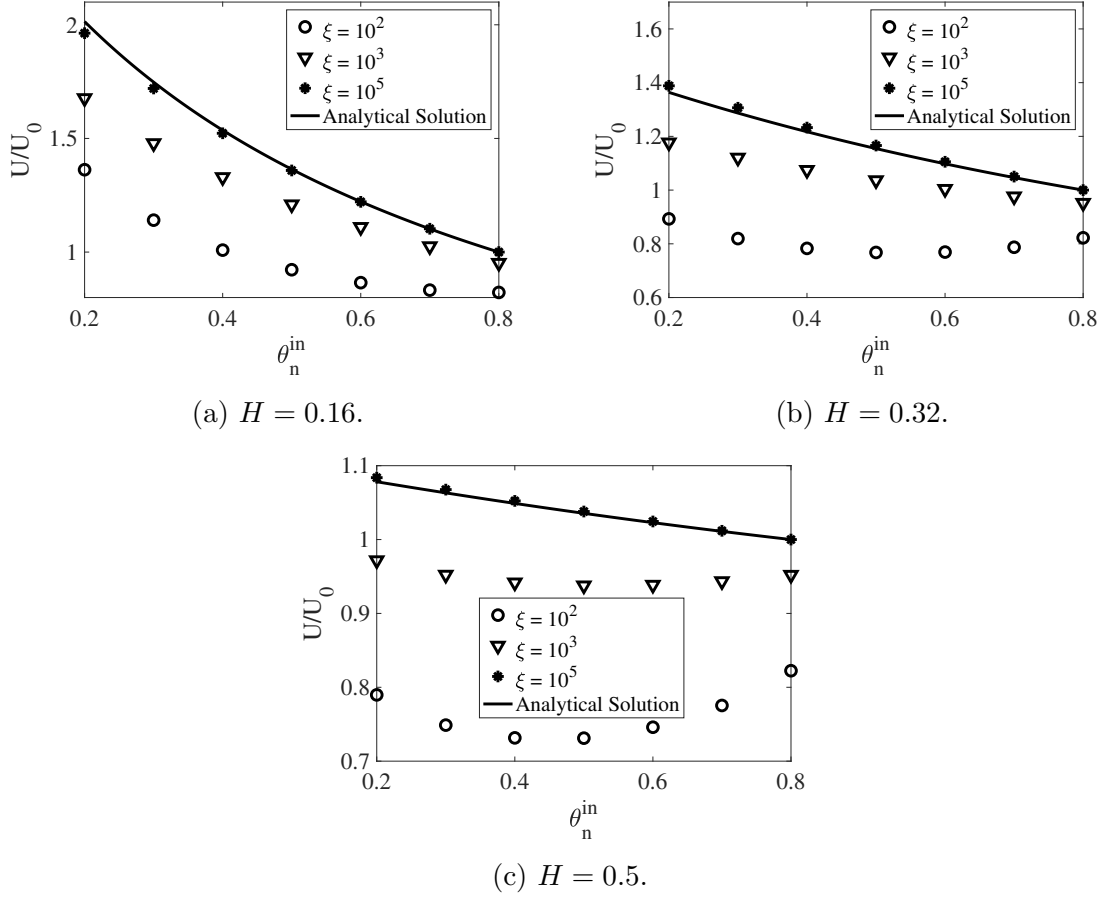


Figure 3.14: The scaled swimming speed vs.  $\theta_n^{\text{in}}$  for different  $H$  and  $\xi$ .  $\beta = 0.25$  and  $\theta_n^{\text{out}} = 0.8$ . The analytical solutions are from [10].

(Figure 3.14c,  $H = 0.5$ ), the swimming speed demonstrates non-monotone variations with the increase of  $\theta_n^{\text{in}}$  for both simulations with the intermediate and small values of  $\xi$ . In these simulations, the swimmer always moves slower in the mixture than in a single fluid.

## 3.2 Locomotion of Finite Swimmer Near Interfaces

### 3.2.1 Problem Setup

For our second model, the swimmer is modeled as a finite inextensible curve with body length  $L = 1$ . For target curvature,  $\kappa_0$ , we choose  $A = 0.12, k = 2\pi$  and  $\omega = 4\pi$ . The computational domain is over the square domain  $[-0.2, 1.8] \times [-1, 1]$ . Periodic boundary conditions are imposed in the  $x$ -direction for all model variables. No-slip conditions are imposed for all velocity components at  $y = \pm 1$ . The size of the computational grid is  $256 \times 256$ . A constant time step of  $\Delta t = 10^{-4}$  is used for all simulations. Each IB object contains 256 IB points. Since the goal of this work is to study locomotion within layers of fluids separated by interfaces, we choose the initial profile of  $\theta_n$  as a piece-wise constant function in the  $y$ -direction:

$$\theta_n(x, y, t = 0) = \begin{cases} \delta\theta_n, & y < H \\ 1 - \delta\theta_n, & y \geq H \end{cases} \quad (3.3)$$

Here, the value of  $H$  which is set to 0.25 for all simulations, defines the initial location of the fluid interface. We choose  $\delta\theta_n = 10^{-4}$  so that the initial value of  $\theta_n$  is slightly above zero near the swimmer and slightly less than 1 for the bulk fluid, making it possible to solve (2.4) and (2.5) numerically. Based on this setup, the fluid interface is implicitly approximated by the spatial distribution of  $\theta_n$ . We choose a large frictional coefficient,  $\xi = 10^{10}$ , so that the two velocity fields,  $\mathbf{u}_n$  and  $\mathbf{u}_s$ , are approximately the same. The viscosity of the solvent fluid in contact with the swimmer is chosen as  $\mu_s = 1$  while the network viscosity,  $\mu_n$ , is varied in the simulations. For all simulations, we use a large tensile stiffness,  $k_s = 10^4$ , so that the length variation of the swimmer is less than 3%. We investigate the movement of two types of swimmers with bending

stiffness values set to 2 and 10. Swimmers with  $k_b = 2$  are referred to as “soft”, while those with  $k_b = 10$  are referred to as “stiff”. Note that for both soft and stiff swimmers, the realized shape is the result of complicated fluid-structure interactions and therefore different from that prescribed by the time-dependent value of  $\kappa_0$ . The swimmer is aligned horizontally at initial time, with the centroid located at  $x = 0.5$ . The net locomotive displacement is in the positive  $x$ -direction, opposite to the traveling wave propagating along the swimmer. We run all simulations up to  $t = 5.0$ . This is 10 periods of the swimming strokes.

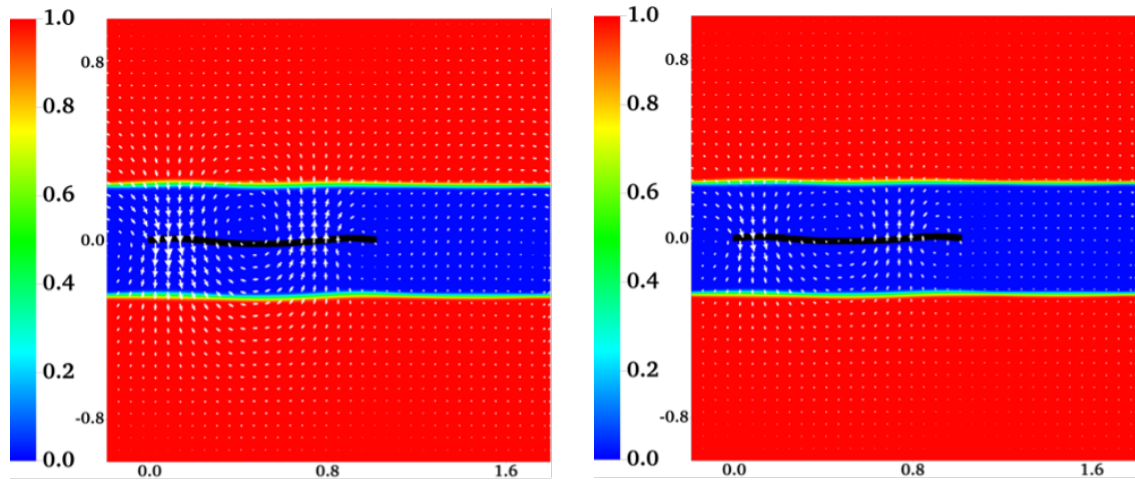
### 3.2.2 Soft Swimmer Near Fluid Interface

First, we study the effect of fluid interfaces on a soft swimmer with bending stiffness  $k_b = 2$ . The results are plotted in Figure 3.15. In Figure 3.15 (a)-(c), the distribution of network volume fraction and the fluid velocity are plotted for three simulations with varying  $\mu_n$  values. For the simulation with  $\mu_n = \mu_s = 1$  (Figure 3.15a), the swimmer essentially moves in a single fluid. As viscosity of the bulk fluid increases from 1 to 5, the fluid velocity is significantly reduced. In simulations with higher values of  $\mu_n$ , the fluid motion is more confined to the inner fluid layer. The perturbation of the interface caused by swimming is also reduced with increased viscosity. As a result of numerical dissipation, the fluid interface is smeared over 2-3 grid blocks during the simulation. The time evolution for the centroid of the swimmer is shown in Figure 3.15d. It is clear that over one stroke (time duration of 0.5), all swimmers exhibit both forward and backward movements. Such movements decrease with the increase of fluid viscosity. Interestingly, despite their very different movements in the forward and backward directions, the centroids of the swimmers with the smallest and intermediate network viscosities coincide approximately at full swimming periods (see the solid and dash-dotted curves in Figure 3.15d). The swimmer that is surrounded by the most viscous

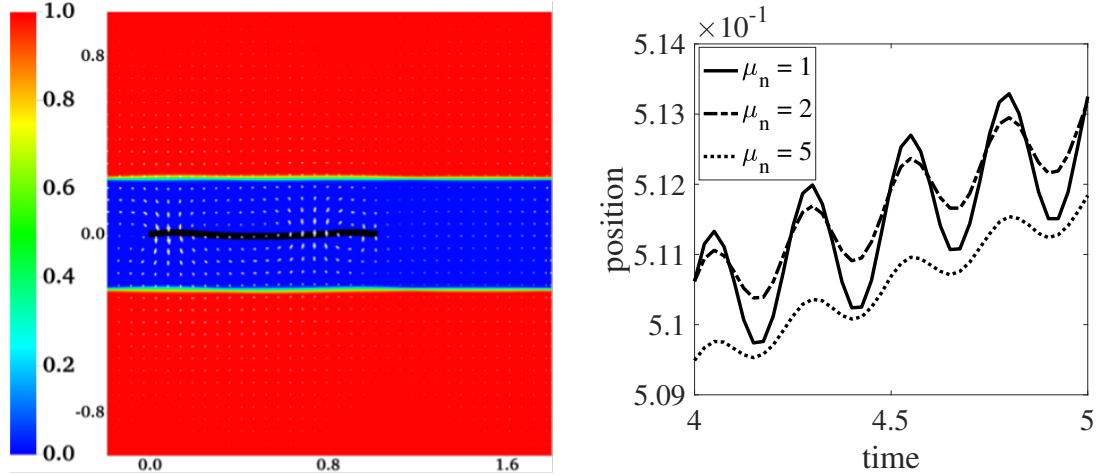
fluid moves the slowest (dotted curve in Figure 3.15d). The swimmer profiles are shown in Figure 3.15e. From this, we see that waving amplitude decreases systematically as viscosity increases.

### 3.2.3 Stiff Swimmer Near Fluid Interface

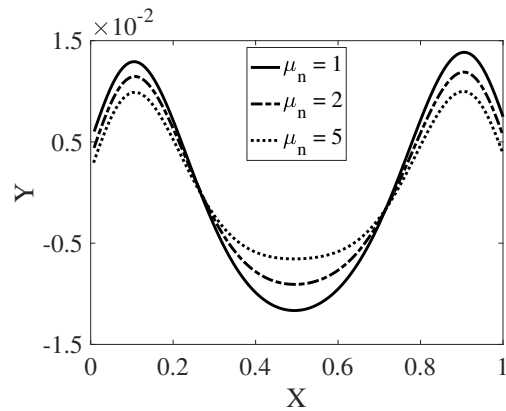
Next, we study the effect of fluid interfaces on a stiff swimmer with bending stiffness  $k_b = 10$ . The results are plotted in Figure 3.16. From the distributions of network volume fraction and fluid velocity in Figure 3.16 (a)-(c), we observe that the body deformation for stiff swimmers is much larger than that for soft swimmers. The undulatory movement of stiff swimmers also drives more significant fluid flow around them, causing larger deformations to the fluid interface. In simulations with larger  $\mu_n$ , we see that there are less deformations of the interface. Figure 3.16, in which the  $x$  component of the swimmer centroid is plotted as a function of time, provides better understanding of the swimming motion. Similar to soft swimmers, stiff swimmers exhibit periodic forward and backward movements. We see in Figure 3.16a over one swimming stroke, the stiff swimmer in a single fluid ( $\mu_n = 1$ ) has the largest forward motion. However, this forward movement is greatly canceled out by a backward slippage of almost the same size resulting in the swimmer moving the slowest. Alternatively, there is considerable decrease in the forward movement of swimmers with larger  $\mu_n$  in the simulations. Despite this effect, the swimming motion is still greatly enhanced by the increase of viscosity due to a more drastic reduction in backward slippage. The swimmer profiles at  $t = 5$  are plotted in Figure 3.16e. Increased fluid viscosity results in reduced waving amplitude of the swimmer, and increased net displacement.



(a)  $\theta_n$  and  $\mu_s$  at time = 2.5,  $\mu_n = 1$ ,  $\|\mu_s\|_{max} = 0.23$  (b)  $\theta_n$  and  $\mu_s$  at time = 2.5,  $\mu_n = 2$ ,  $\|\mu_s\|_{max} = 0.17$

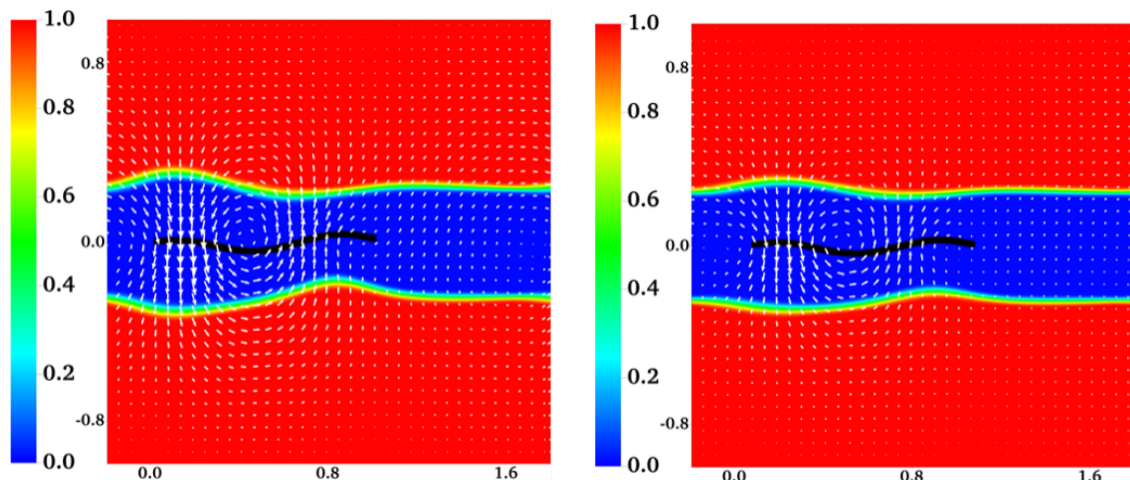


(c)  $\theta_n$  and  $\mu_s$  at time = 2.5,  $\mu_n = 5$ ,  $\|\mu_s\|_{max} = 0.13$  (d) The horizontal position for the centroid of the swimmer at different times.

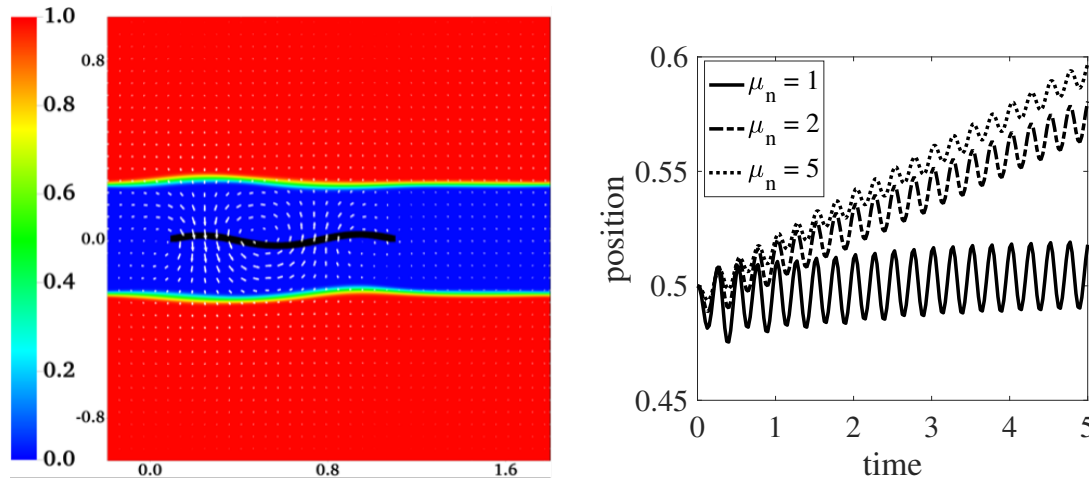


(e) Comparison of swimmer profiles. All vectors have the same scale.

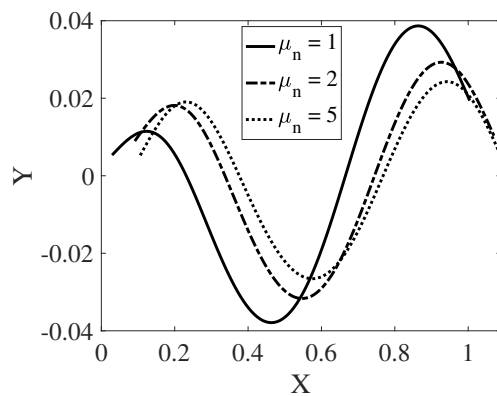
Figure 3.15: Soft Swimmer



(a)  $\theta_n$  and  $\mu_s$  at time = 5,  $\mu_n = 1$ ,  $\|\mu_s\|_{max} = 0.93$  (b)  $\theta_n$  and  $\mu_s$  at time = 5,  $\mu_n = 2$ ,  $\|\mu_s\|_{max} = 0.69$



(c)  $\theta_n$  and  $\mu_s$  at time = 5,  $\mu_n = 5$ ,  $\|\mu_s\|_{max} = 0.48$  (d) The horizontal position for the centroid of the swimmer at different times.



(e) Comparison of swimmer profiles. All vectors have the same scale.

Figure 3.16: Stiff Swimmer

# Chapter 4

## Conclusion

In our work, we have conducted a computational investigation of the classical swimming sheet problem within heterogeneous media, utilizing a two-fluid mixture model and the Immersed Boundary Method. The swimmer moves in a low-viscosity region surrounded by a more viscous bulk fluid, with different fluid layers separated by interfaces. When dealing with the scenario in which the volume fraction of one fluid vanishes in part of the domain, we utilize numerical regularization to solve the model equations. The mixture model and numerical regularization eliminates the necessity to explicitly track the interface and enforce the interface conditions. This significantly simplifies the computational algorithm, particularly for problems involving dynamic interfaces. Our numerical simulations closely align with analytical results for locomotion in layers of single phase fluids. To the best of our knowledge, this is the first time that such problems are simulated by a combination of the IB method and the interface-capturing strategy. Our numerical findings reveal that both the thrust and the drag on the swimmer increase with the increased viscosity differences between fluid layers and the decrease of the interface-swimmer distance. The rate of increment for the thrust is greater than that for the drag. This always leads to faster swimming, an effect more

substantial for swimmers near non-deformable interfaces.

We also explore the locomotion of swimmers within layers of fluid mixtures. Relative motion and phase separation between components in the mixture can be induced by the waving swimmer. The results reveal that the swimming speed depends in a non-trivial way on several parameters. With other conditions being the same, greater frictional forces lead to reduced relative motion and phase separation within the mixture. This always makes the swimmer move faster. For swimming in close proximity to the interface, the confinement effect dominates. The reduction of viscosity for the mixture near the swimmer, achieved by the increase of  $\theta_s$  or the decrease of  $\theta_n$ , strengthens the confinement effect from the surrounding bulk fluid, leading to an acceleration in swimming motion. The situation is more complicated, however, if the interfaces are further away from the swimmer. Depending on the values of  $H$  and  $\xi$ , lowering the network fraction near the swimmer can either enhance or reduce the swimming speed. Consequently, swimmers in a two-fluid mixture near free interfaces may move faster or slower than those in a single fluid, contingent on their distance from the interface, the composition of the fluid mixture, as well as the magnitude of the frictional force between components in the mixture. This observation can be potentially related to the disparity of experimental results on microorganism swimming [34, 17].

Our work also investigates the locomotion of an undulatory swimmer with finite length within a low-viscosity fluid surrounded by a more viscous bulk flow. Rather than moving with a prescribed swimming gait, the swimmer's movement is actuated by a prescribed active body moment density. Our simulation results demonstrate that near a fluid interface, significant swimming enhancement is achieved only for relatively stiff swimmers. It is well known that locomotive speed-ups near fluid interfaces are a result of the confinement effect provided by the surrounding bulk fluid. As the viscosity difference between the two fluids separated by the interface increases,

the confinement effect strengthens. This allows a swimmer to induce greater fluid vorticity for increased swimming speed. As a result, in the vicinity of a fluid interface, swimmers with prescribed gaits always move faster with an increased viscosity ratio  $\frac{\mu_n}{\mu_s}$ . Conversely, stronger confinement, attributed to an increase in  $\mu_n$ , typically hinders the swimming motion by reducing the beating amplitude of an active swimmer with a given body moment density. The speed-up or slow-down of the swimmer is contingent on the interplay between these two effects. Our simulations demonstrate that the effect of the fluid interface in favor of swimming dominates exclusively for stiff swimmers.

The computational framework presented in the paper can be applied to the study of the locomotion of microorganisms within various biofluid media, especially for the cases where swimmers are in close proximity to free deformable interfaces. The versatility of the method also makes it a suitable tool to investigate problems in which structural properties of the fluid media are altered by the dynamic of the swimmer. For instance, a notable observation is the phase transition of gastric mucin from a viscoelastic gel to a viscous solution, triggered by the urease production from the ulcer-causing pathogen *H. pylori* [6]. This localized de-gelling process allows the bacterium to navigate through a fluidic pocket, surrounded by gel, and cause infection. While prior analytical work in [27], based on a simplified model, highlights the significance of the role of the size of the fluid zone in determining the physics of motility, it overlooks the dynamics of the gel-sol transition, chemical reactions, and mucus transport. Further expansion of our computational model can provide a comprehensive framework for the investigation of such locomotive problems in multi-fluid heterogeneous media. The kinetics of rheological changes for gastric mucus may be modeled through the choice of appropriate functional forms for the network stress tensor, which are dependent on the deformation history and chemical concentrations. The process of mucin degradation can be simulated through the addition of reaction terms in equations for  $\theta_n$  and  $\theta_s$ .

In addition to viscosity differences and bending stiffness, it would be interesting to conduct a systematic investigation into the influences of other model parameters, such as interface position and target curvature. Expanding on our model could shed light on how these factors interact with a change in swimmer alignment. For instance, instead of the conventional horizontal swimmer alignment parallel to the interface, we can explore a vertical alignment that is perpendicular to the interface. Furthermore, our computational model can be extended to study locomotion problems near interfaces in viscoelastic fluids. Such problems have significant biological implications as they relate to bacterial motility and infection. Finally, it would be interesting to apply an implicit time-stepping method to improve the computational efficiency of our work and explore the potential benefits of this type of method.

# Bibliography

- [1] R. Bansil, J.P. Celli, J.M. Hardcastle, and B.S. Turner. The influence of mucus microstructure and rheology in helicobacter pylori infection. *Front. Immunol.*, 4:310, 2013.
- [2] J. Bastos-Arrieta, A. Revilla-Guarinos, W.E. Uspal, and J. Simmchen. Bacterial biohybrid microswimmers. *Front Robot AI*, 5(97), 2018.
- [3] S. Boryshpolets, J. Cosson, V. Bondarenko, E. Gillies, M. Rodina, B. Dzyuba, and O. Linhart. Different swimming behaviors of sterlet (*Acipenser ruthenus*) spermatazoa close to solid and free surfaces. *Theriogenology*, 79(1):81–86, 2013.
- [4] A. Cartwright and J. Du. Low reynolds number swimming near interfaces in multi-fluid media. *Appl. Sci.*, 11(19):9109, 2021.
- [5] A. Cartwright and J. Du. Enhancement of active swimming near fluid interfaces. *J. Phys.: Conf. Ser.*, 2224:012034, 2022.
- [6] J.P. Celli, B.S. Turner, N.H. Afdhal, S. Keates, I. Ghiran, C.P. Kelly, R.H. Ewoldt, G.H. McKinley, P. So, S. Erramilli, and R. Bansil. Helicobacter pylori moves through mucus by reducing mucin viscoelasticity. *Proc. Natl. Acad. Sci.*, 106(34):14321–6, 2009.

- [7] J.C. Crispell, L.J. Fauci, and M. Shelley. An actuated elastic sheet interacting with passive and active structures in a viscoelastic fluid. *Phys. Fluids*, 25(1):013103, 2013.
- [8] N.G. Cogan and R.D. Guy. Multiphase flow models of biogels from crawling cells to bacterial biofilms. *HFSP J*, 4(1):11–25, 2010.
- [9] P. Colella. Multidimensional upwind methods for hyperbolic conservation laws. *J. Comput. Phys.*, 87(1):171–200, 1990.
- [10] M. Dias and T. Powers. Swimming near deformable membranes at low reynolds number. *Phys. Fluids*, 25:101901, 2013.
- [11] W.R. DiLuzio, L. Turner, M. Mayer, P. Garstecki, D.B. Weibel, H.C. Berg, and G.M. Whitesides. Escherichia coli swim on the right-hand side. *Nature*, 435:1271–1274, 2005.
- [12] J. Du and A.L. Fogelson. A two-phase mixture model of platelet aggregation. *Math. Med. Biol.*, 35(2):225–256, 2018.
- [13] J. Du, R.D. Guy, and A.L. Fogelson. An immersed boundary method for two-fluid mixtures. *J. Comput. Phys.*, 262:231–243, 2014.
- [14] J. Du, R.D. Guy, A.L. Fogelson, G.B. Wright, and J.P. Keener. An interface-capturing regularization method for solving the equations for two-fluid mixtures. *Commun. Comput. Phys.*, 14(5):1322–1346, 2013.
- [15] J. Du, J.P. Keener, R.D. Guy, and A.L. Fogelson. Low reynolds-number swimming in viscous two-phase fluids. *Phys. Rev. E*, 85(3 Pt 2):036304, 2012.

- [16] G.J. Elfring and E. Lauga. Theory of locomotion through complex fluids. *Complex Fluids in Biological Systems*, Spagnolie, S.E., Ed.; Springer: New York, NY, USA:283–317, 2015.
- [17] J. Espinosa-Garcia, E. Lauga, and R. Zenit. Fluid elasticity increases the locomotion of flexible swimmers. *Phys. Fluids*, 25(3):031701, 2013.
- [18] A.L. Fogelson and R.D. Guy. Immersed-boundary-type models of intravascular platelet aggregation. *Comput. Method Appl. Mech. Eng.*, 197(25-28):2087–2104, 2008.
- [19] S. Gomez, F.A. Godinze, E. Lauga, and R. Zenit. Helical propulsion in shear-thinning fluids. *J. Fluid Mech.*, 812(R3), 2017.
- [20] B.E. Griffith, X. Luo, D.M. McQueen, and C.S. Peskin. Simulating the fluid dynamics of natural and prosthetic heart valves using the immersed boundary method. *Int. J. Appl. Mech.*, 1(1):137–177, 2009.
- [21] R.D. Guy and B. Thomases. Computational challenges for simulating strongly elastic flows in biology. *Complex Fluids in Biological Systems*, Spagnolie, S.E., Ed.; Springer: New York, NY, USA:359–397, 2015.
- [22] E. Lauga, W.R. DiLuzio, G.M. Whitesides, and H.A. Stone. Swimming in circles: Motion of bacteria near solid boundaries. *Biophys. J.*, 90(2):400–12, 2006.
- [23] E. Lauga and T.R. Powers. The hydrodynamics of swimming microorganisms. *Rep. Prog. Phys.*, 72(9):096601, 2009.
- [24] P. Lee and C.W. Wolgemuth. An immersed boundary method for two-phase fluids and gels and the swimming of *c. elegans* through viscoelastic fluids. *Phys. Fluids*, 28(1):011901, 2016.

- [25] G. Li, E. Lauga, and A.M. Ardekani. Microswimming in viscoelastic fluids. *J. Non-Newton. Fluid Mech.*, 297:104655, 2021.
- [26] Y. Man and E. Lauga. Phase-separation models for swimming enhancement in complex fluids. *Phys. Rev. E*, 92(2):023004, 2015.
- [27] S.A. Mirbagheri and H.C. Fu. Helicobacter pylori couples motility and diffusion to actively create a heterogeneous complex medium in gastric mucus. *Phys. Rev. Lett.*, 116(19):198101, 2016.
- [28] E.P. Newren, A.L. Fogelson, R.D. Guy, and R.M. Kirby. Unconditionally stable discretizations of the immersed boundary equations. *J. Comput. Phys.*, 222(2):702–719, 2007.
- [29] H. Nganguia, L. Zhu, D. Palaniappan, and O. Pak. Squirring in a viscous fluid enclosed by a brinkman medium. *Phys. Rev. E*, 101(6):063105, 2020.
- [30] A.E. Patteson, A. Gopinath, M. Goulian, and P.E. Arratia. Running and tumbling with e. coli in polymeric solutions. *Sci. Rep.*, 5:15761, 2015.
- [31] C.S. Peskin. The immersed boundary method. *Acta Numer.*, 11:479–517, 2002.
- [32] E.E. Riley and E. Lauga. Enhanced active swimming in viscoelastic fluids. *EPL*, 108(3):34003, 2014.
- [33] V. Shaik and A. Ardekani. Swimming sheet near a plane surfactant-laden interface. *Phys. Rev. E*, 99(3):033101, 2019.
- [34] X.N. Shen and P.E. Arratia. Undulatory swimming in viscoelastic fluids. *Phys. Rev. Lett.*, 106(20):208101, 2011.

- [35] W. Strychalski and R.D. Guy. A computational model of bleb formation. *Math. Med. Biol. J. IMA*, 30(2):115–130, 2013.
- [36] J. Sznitman and P.E. Arratia. Locomotion through complex fluids: An experimental view. *Complex Fluids in Biological Systems*, Spagnolie, S.E., Ed.; Springer: New York, NY, USA:245–281, 2015.
- [37] G.I. Taylor. Analysis of the swimming of microscopic organisms. *Proc. R. Soc. A*, 209(1099):447–461, 1951.
- [38] J. Teran, L. Fauci, and M. Shelley. Viscoelastic fluid response can increase the speed and efficiency of a free swimmer. *Phys. Rev. Lett.*, 104(3):038101, 2010.
- [39] B. Thomases and R.D. Guy. Mechanisms of elastic enhancement and hindrance for finite length undulatory swimmers in viscoelastic fluids. *Phys. Rev. Lett.*, 113(9):098102, 2014.
- [40] S.O. Unverdi and G. Tryggvason. A front tracking method for viscous incompressible multi-fluid flows. *J. Comput. Phys.*, 100(1):25–37, 1992.
- [41] G.B. Wright, R.D. Guy, J. Du, and A.L. Fogelson. A high-resolution finite-difference method for simulating two-fluid, viscoelastic gel dynamics. *J. Non-Newton. Fluid Mech.*, 166(19-20):1137–1157, 2011.